J. Fluid Mech. (2007), *vol.* 570, *pp.* 253–296.
doi:10.1017/S0022112006003053 Printed in the United Kingdom

A numerical investigation of the Stokes boundary layer in the turbulent regime

By S. SALON[1,2], V. ARMENIO[1]† AND A. CRISE[2]

[1]Dipartimento di Ingegneria Civile e Ambientale, Università degli Studi di Trieste, Trieste, Italy
[2]Istituto Nazionale di Oceanografia e di Geofisica Sperimentale – OGS, Sgonico, Italy

(Received 11 August 2005 and in revised form 7 June 2006)

The Stokes boundary layer in the turbulent regime is investigated by using large-eddy simulations (LES). The Reynolds number, based on the thickness of the Stokes boundary layer, is set equal to $Re_\delta = 1790$, which corresponds to test 8 of the experimental study of Jensen *et al.* (*J. Fluid Mech.* vol. 206, 1989, p. 265).

Our results corroborate and extend the findings of relevant experimental studies: the alternating phases of acceleration and deceleration are correctly reproduced, as is the sharp transition to turbulence, observable at a phase angle between 30° and 45°, and its maximum between 90° and 105°. Overall, a very good agreement was found between our LES first- and second-order turbulent statistics and those of Jensen *et al.* (1989). Some discrepancies were observed when comparing turbulent intensities in the phases of the cycle characterized by a low level of turbulent activity.

In the central part of the cycle, namely from the mid acceleration to the late deceleration phases, fully developed equilibrium turbulence is present in the flow field, and the boundary layer resembles that of a canonical, steady, wall-bounded flow. In those phases characterized by low turbulent activity, two separate regions can be detected in the flow field: a near-wall one, where the vertical turbulent kinetic energy varies much more rapidly than the other two components, thus giving rise to the formation of horizontal, pancake-like turbulence; and an outer region where both vertical and spanwise velocity fluctuations vary much faster than the streamwise ones, hence producing cigar-like turbulence.

As a side result, the range of application of the plane-averaged dynamic mixed model was assessed based on the qualitative behaviour over the cycle of a significant parameter representing the ratio between a turbulent time scale and a free-stream time scale associated with the oscillatory motion.

1. Introduction

The study of oscillating boundary layers represents an intriguing challenge in fully understanding unsteadily driven turbulent flows. Despite the relevance of unsteady turbulent boundary layers in many disciplines (coastal and offshore engineering, biofluiddynamics, geophysical flows, just to cite some applications), most of the research has been concerned with steady flows. Comparatively few investigations have been devoted to the analysis of wall turbulence in unsteady flows.

† Author to whom correspondence should be addressed: armenio@dic.units.it

In the Stokes boundary layer, a zero-mean harmonic velocity field drives the flow, and the Reynolds number

$$Re_\delta = \frac{U_0 \delta_S}{\nu}$$

is commonly defined by means of the maximum amplitude of the outer velocity U_0 and the Stokes-layer thickness $\delta_S = \sqrt{2\nu/\omega}$, where ν is the kinematic viscosity of the fluid and ω the angular frequency of the oscillations.

Experimental investigations (Hino, Sawamoto & Takasu 1976; Hino *et al.* 1983; Jensen, Sumer & Fredsøe 1989; Akhavan, Kamm & Shapiro 1991*a*; Sarpkaya 1993) have showed that the Stokes boundary layer experiences four different flow regimes, depending on the value of Re_δ: the laminar regime (L), the disturbed laminar regime (DL), the intermittent turbulent regime (IT) and the fully developed turbulent regime (T). In other words, as pointed out by Jensen *et al.* (1989, henceforth referred to as JSF89), every phase of the cycle undergoes the different flow regimes with increasing Re_δ. At small values of Re_δ turbulence first appears at the beginning of the decelerating phase, associated with the presence of explosive near-wall bursts (Hino *et al.* 1983); as Re_δ increases turbulence is involved in earlier and earlier phases of the cycle. The laminar regime holds for Re_δ smaller than around 100; for Re_δ roughly between 100 and 500–550 there is the disturbed laminar regime, characterized by the presence of small-amplitude perturbations, imposed onto the base Stokes flow. As Re_δ becomes larger than 550, the two-dimensional pattern typical of the disturbed laminar regime becomes a three-dimensional one and the flow moves to the intermittent regime, where explosive turbulence bursts are created during the decelerating phases of the cycle. A detailed discussion on these regimes can be found in Blondeaux & Seminara (1979), Akhavan, Kamm & Shapiro (1991*b*), Vittori & Verzicco (1998). Fully developed turbulence is present during the cycle only in the turbulent regime: according to the experimental analysis by Hino *et al.* (1983) such a regime exists for $Re_\delta > 800$; Sarpkaya (1993) and JSF89 clearly showed that at $Re_\delta \sim 1800$ fully developed turbulence is already present during most of the cycle of oscillation; moreover, fully developed turbulence has been recorded throughout the cycle for $Re_\delta \geqslant 3460$ (see JSF89).

Recent studies of oscillating boundary layers have been focused on the DL and the IT regimes (Spalart & Baldwin 1987; Akhavan *et al.* 1991*b*; Vittori & Verzicco 1998; Costamagna, Vittori & Blondeaux 2003) by means of direct numerical simulations (DNS). Although computations at Re_δ as large as 1120 have been attempted, reliable DNS have been carried out up to $Re_\delta \sim 800$ (in the IT regime), aimed at understanding the mechanism triggering transition to turbulence and the evolution over the cycle of the near-wall turbulence structures (for details see Vittori & Verzicco 1998; Costamagna *et al.* 2003). Direct numerical simulations of the Stokes boundary layer in the turbulent regime have not been carried out as yet, due to prohibitive computational costs as also observed by Costamagna *et al.* (2003).

Over the last decade, large-eddy simulation (LES) has proved able to simulate accurately equilibrium as well as non-equilibrium turbulent flows (Sarghini, Piomelli & Balaras 1999; Wu & Squires 1998; Henn & Sykes 1999; Falcomer & Armenio 2002). Moreover LES, used in conjunction with dynamic subgrid-scale models, has also been demonstrated to simulate correctly flow fields characterized by sharp transition

to turbulence and local re-laminarization (see for example Germano *et al.* 1991; Meneveau, Lund & Cabot 1996; Armenio & Sarkar 2002). For turbulent flows subjected to periodic forcing, LES was successfully employed by Scotti & Piomelli (2001) to study pulsating flow in a channel. Although there are some similarities between the simulations of Scotti & Piomelli (2001) in the limit of the low-frequency regime and the cases studied in the present research (similarities that will be exploited in the next sections), as also discussed in Lodahl, Sumer & Fredsøe (1998) the flow field analysed herein profoundly differs from the pulsating case. However, Scotti & Piomelli (2001) showed that LES used in conjunction with a dynamic eddy-viscosity subgrid-scale model is suitable for the investigation of unsteady periodic turbulent flows which exhibit phases where the flow is in laminar conditions and phases where sharp transition to turbulence occurs.

Large-eddy simulations of the Stokes boundary layer have been carried out by Hsu, Lu & Kwan (2000) and by Lohmann *et al.* (2006). In the study of Hsu *et al.* (2000), the results of an LES carried out with a dynamic eddy viscosity model were compared with those of a simulation performed using the Reynolds-averaged equations (RANS). The LES model was able to reproduce the reduction of the phase lag between the wall shear stress and the free-stream oscillation occurring with increasing values of the Reynolds number and to give a reasonable estimation of the maximum value of the friction coefficient when compared to the experimental data of Kamphuis (1975). However, the LES in the IT regime (at $Re_\delta = 864$) was not able to capture the characteristic, triangular-shaped evolution of the wall shear stress over a half-cycle (compare for example their figure 9 with figure 5 of Costamagna *et al.* (2003) and also with our figure 21). Comparisons with available experimental turbulent statistics were not given.

Lohmann *et al.* (2006) used the classical model of Smagorinsky (1963) to investigate a ventilated Stokes boundary layer in the fully developed regime at $Re_\delta = 3464$. Simulations were also carried out in an unventilated case (that considered in the present paper) and results compared with the reference data of JSF89. An overall reasonable agreement with the experimental data of JSF89 was obtained, in particular the friction coefficient was overestimated by only 4 % when compared to that in JSF89. However, noticeable differences were found in the time evolution of the wall shear stress and in the first- and second-order statistics, because the grid spacing used by Lohmann *et al.* was not small enough to solve properly the near-wall streaks.

In the present paper we simulate the Stokes boundary layer in the turbulent regime, at a value of the Reynolds number such that most of the cycle of oscillation experiences fully developed turbulence. Owing to the large value of the Reynolds number required for a simulation in the T regime, DNS are not feasible and thus we used *resolved* (the concept will be explored in the next section) large-eddy simulation, in conjunction with a dynamic mixed model (DMM). The aim of the present study is to supply insights into the characteristics of the flow field in the turbulent regime, also in comparison to the experimental investigations of JSF89.

The paper is organized as follows: in the next section we formulate the problem together with the mathematical model adopted and we give an overview of the simulations carried out. Section 3 contains the results of our simulations and comparisons to the relevant literature. Section 4 deals with the performance of the DMM in two different regimes, namely the T regime discussed throughout the paper and the IT regime at $Re_\delta = 990$. Concluding remarks are given in § 5.

2. The problem formulation

We investigate an oscillatory flow driven by an harmonic pressure gradient in the x-direction:

$$\frac{\mathrm{d}P_d}{\mathrm{d}x_d}(t_d) = -U_0\omega\cos(\omega t_d) \tag{2.1}$$

where P_d is the dimensional kinematic pressure (i.e. pressure divided by the fluid density ρ_0), U_0 and ω are defined in the previous section, t_d and x_d are respectively the time and the streamwise direction, namely that along which the oscillation develops. Henceforth the index d denotes dimensional variables. The pressure gradient defined above gives the following free-stream velocity:

$$U_d(t_d) = U_0\sin(\omega t_d).$$

In their experimental study, JSF89 considered a large-scale Reynolds number defined as $Re = aU_0/\nu$ where $a = U_0/\omega$ is the amplitude of the free-stream motion (the amplitude of the sinusoidal motion of a fluid parcel moving in the free-stream region) and ν is the kinematic viscosity, observing that a fully developed turbulent regime appears for $Re \geqslant 1.6\times10^6$. Within this regime JSF89 investigated values of Reynolds number up to 6×10^6. Since

$$Re = \frac{Re_\delta^2}{2}$$

the following range of values was studied in the turbulent regime:

$$1790 \leqslant Re_\delta \leqslant 3464.$$

In the present paper we reproduce test 8 (as reported in table 1 of JSF89), which is for $Re = 1.6\times10^6$ corresponding to $Re_\delta = 1790$. As already discussed, according to Sarpkaya (1993) at this Reynolds number turbulence is present in most of the cycle. As we clearly show in the next section, in making the choice of the Reynolds number of the simulation a compromise had to be reached between the need to simulate a value of Re large enough to lie within the T regime and the computational requirements for a *resolved* LES, namely a simulation where the near-wall streaks are solved directly.

2.1. *The mathematical model*

In LES, the large, energy-carrying scales of motion are resolved directly, whereas the small, more isotropic and dissipative scales are parameterized by means of a sub-grid-scale model. The filtered, non-dimensional equations governing the oscillating boundary layer driven by an harmonic pressure gradient are

$$\frac{\partial\bar{u}_i}{\partial x_i} = 0, \tag{2.2}$$

$$\frac{\partial\bar{u}_i}{\partial t} + \frac{\partial\bar{u}_j\bar{u}_i}{\partial x_j} = -\frac{\partial\bar{p}}{\partial x_i} + \frac{1}{Re}\frac{\partial}{\partial x_j}\frac{\partial\bar{u}_i}{\partial x_j} + \cos(t)\delta_{i1} - \frac{\partial\tau_{ij}}{\partial x_j}. \tag{2.3}$$

In (2.2) and (2.3), an overbar denotes the filtering operation, the coordinate x_i (hereafter x_1, x_2, x_3 or x, y, z are used interchangeably for the streamwise, spanwise and wall-normal directions) is made non-dimensional with the amplitude of motion a, t is the time coordinate made non-dimensional with $1/\omega$, $\bar{u}_i$ is the i-component of the filtered velocity field (u_1, u_2, u_3 or u, v, w are used for the streamwise, spanwise and wall-normal velocity components), made non-dimensional with U_0, $\bar{p}$ is the filtered pressure field made non-dimensional with $\rho_0{U_0}^2$.

The term

$$\tau_{ij} = (\overline{\overline{u}_i \overline{u}}_j - \overline{\overline{u}}_i \overline{\overline{u}}_j) - 2C\overline{\Delta}^2 |\overline{\boldsymbol{S}}| \overline{S}_{ij} \tag{2.4}$$

represents the subgrid-scale (SGS) stresses that are parameterized by means of a dynamic mixed model composed of an anisotropic scale-similar part (Bardina *et al.* 1980) and an eddy viscosity part (Smagorinsky 1963). In (2.4) C is the constant of the eddy viscosity part of the model, $\overline{\Delta}$ is the filter width, $\overline{S}_{ij}$ are the elements of the resolved strain rate tensor and $|\overline{\boldsymbol{S}}| = \sqrt{2\overline{S}_{ij}\overline{S}_{ij}}$. The model was implemented following the mathematically consistent formulation of Vreman, Guerts & Kuerten (1994). The constant C is evaluated using the least-square procedure of Lilly (1992):

$$C = -\frac{1}{2} \frac{\langle L_{ij} M_{ij} \rangle - \langle N_{ij} M_{ij} \rangle}{\langle M_{mn} M_{mn} \rangle} \tag{2.5}$$

where $\langle . \rangle$ represents an appropriate ensemble averaging required to avoid the mathematical inconsistency associated with the extraction of the constant C from a filtering operation. We average the terms of (2.5) over the (x, y) planes of homogeneity. The model is recast in a contravariant form following Armenio & Piomelli (2000). In (2.5)

$$L_{ij} = \Sigma_{ij} - \widehat{\tau}_{ij} = \widehat{\overline{u}_i \overline{u}}_j - \widehat{\overline{u}}_i \widehat{\overline{u}}_j$$

is the resolved turbulent stress tensor, Σ_{ij} is the subtest-scale stress tensor and a hat denotes the explicit filtering operation carried out at the test level. The other terms of (2.5) are respectively

$$M_{ij} = \widehat{\overline{\Delta}}^2 |\widehat{\overline{\boldsymbol{S}}}| \widehat{\overline{S}}_{ij} - \widehat{\overline{\Delta}^2 \overline{S} \overline{S}}_{ij}, \tag{2.6}$$

$$N_{ij} = (\widehat{\overline{\overline{u}_i \overline{u}}}_j - \widehat{\overline{\overline{u}}}_i \widehat{\overline{\overline{u}}}_j) - (\widehat{\overline{u}_i \overline{u}}_j - \widehat{\overline{u}}_i \widehat{\overline{u}}_j). \tag{2.7}$$

Consistently with the use of a top-hat filter (Lund 1997), the value $\sqrt{6}$ was used for the filter width ratio $\widehat{\overline{\Delta}}/\overline{\Delta}$. Finally, filtering was performed in three directions, in the computational space (see Armenio & Piomelli 2000). A detailed discussion on the mathematical formulation of the model and its performance is given in Armenio & Piomelli (2000) and is not repeated here. Our LES is applied without any explicit filtering at the cutoff. The literature supports this choice: see among others Wu & Squires (1998), Ding & Street (2003), Cui & Street (2001), Calhoun & Street (2001), Henn & Sykes (1999). In particular, these studies have clearly demonstrated the good performance of the SGS models even when used in conjunction with second-order space accuracy.

Explicit filtering was attempted to isolate the effect of filtering from truncation error of the numerical scheme. For second-order finite difference schemes, Lund & Kaltenbach (1995) found that explicit filtering improves LES results, although more accurate results (at a smaller computational cost) were achieved by mesh refinement without explicit filtering. Similar conclusions were drawn in the recent study of Gullbrand & Chow (2003). Specifically, they showed that the advantages of the use of explicit filtering, that on the other hand is computationally very expensive, are progressively lost when the grid size is able to resolve the important physical characteristics of the flow and to obtain a solution that is not greatly affected by numerical error. This is the strategy accomplished in the present work.

2.2. *The numerical method and the boundary conditions*

Equations (2.2) and (2.3) are solved by means of the semi-implicit, fractional-step method of Zang, Street & Koseff (1994). The convective terms are integrated in time using the Adams–Bashforth technique, the diffusive terms are treated implicitly by the use of the Crank–Nicolson scheme. The spatial derivatives are discretized with a second-order centred scheme. The Poisson equation for the pressure field is solved with a multigrid technique. Overall, the algorithm is second-order accurate both in time and in space. The algorithm, together with the SGS model, has been used for the analysis of a wide variety of steady non-equilibrium turbulent flows (see for example Armenio & Piomelli 2000; Falcomer & Armenio 2002) and steady flows characterized by local re-laminarization and sharp re-transition to turbulence (Armenio & Sarkar 2002; Armenio & Sarkar 2004).

A no-slip boundary condition is enforced at the bottom wall and a free-slip condition at the top boundary, while, since turbulence is homogeneous in the streamwise and spanwise directions, periodic boundary conditions are taken there.

As initial condition we first started a simulation using a steady, driving pressure gradient with non-dimensional amplitude equal to -1 and, after a turbulent field had developed, we removed the mean velocity field, holding the fluctuating three-dimensional components, and started the oscillatory motion. The use of such an initialization technique has saved a large amount of CPU time, compared to the case of a simulation started from a fluid at rest that thus has to develop through the flow regimes discussed in the previous section. The statistics were accumulated by averaging over the (x, y)-planes of homogeneity, and in phase over half-cycle (thereby referred to as ensemble-averaging) taking advantage of the fact that the flow field repeats every half-cycle with the sign of the mean streamwise velocity reversed. The data from the first cycle of oscillation were not used for the evaluation of the statistics, since they could have been affected by the initial conditions. We have accumulated the statistics over 15 complete cycles, thus using 30 half-cycles for each phase of the oscillation.

The computational effort needed for the simulation of the present flow has required the implementation of a parallel version of the code. The parallel-programming paradigm adopted is the Message Passing Interface standard (MPI), developed by the domain decomposition strategy.

2.3. *Computational requirements*

It is well recognized that the main requirement for an accurate LES is that the near-wall turbulent structures be solved properly. In canonical boundary layers it is well established that the near-wall streaks are elongated in the direction of motion, extending for about 1000 and 100 wall units respectively in the streamwise and spanwise directions (Pope 2000). The direct resolution of such structures requires the maximum grid spacing in the streamwise and spanwise directions to be respectively $\Delta x^+ = \Delta x_d/z^* \approx 60$, $\Delta y^+ = \Delta y_d/z^* \approx 20$ where $z^* = \nu/u_\tau$ is the wall unit; $u_\tau = \sqrt{\tau_w/\rho_0}$ denotes the friction velocity, where τ_w is the wall shear stress (for an exhaustive discussion the reader is referred to Piomelli & Balaras 2002). A large-eddy simulation that does not fulfil such a requirement is not able to resolve the near-wall, large-scale structures and consequently tends to wrongly estimate the wall shear stress.

In the oscillatory flow problem, the wall shear stress varies in time over the cycle, and the maximum is reached around the end of the acceleration phase. To evaluate the wall unit z^* we used the maximum value of the wall shear stress as measured in test 8 of JSF89 (the value $U_{fm} = 4.8\,\mathrm{cm\,s^{-1}}$ read from their table 1, has been appropriately scaled over our numerical parameters).

	$L_x/\delta_S, L_y/\delta_S, L_z/\delta_S$	$n_x \times n_y \times n_z$	$\Delta x^+, \Delta y^+, \Delta z^+_{min}, \Delta z^+_{max}$	ϵ
C1	50, 25, 40	$64 \times 32 \times 256$	62, 62, 2, 22	0
C2	50, 25, 40	$64 \times 64 \times 256$	62, 31, 2, 22	0
C3	50, 25, 40	$64 \times 96 \times 256$	62, 21, 2, 22	0
C4	50, 25, 40	$96 \times 96 \times 256$	41, 21, 2, 22	0
C5	50, 25, 40	$64 \times 96 \times 400$	62, 21, 1, 20	0
C6	50, 25, 40	$64 \times 96 \times 256$	62, 21, 2, 22	0.005
C7	50, 25, 80	$64 \times 64 \times 512$	62, 31, 2, 22	0

TABLE 1. Computational parameters of the simulations at $Re_\delta = 1790$. The non-dimensional grid spacing is referred to the maximum wall shear stress over the period and consequently to the minimum value of the wall unit $z^* = \nu/u_\tau$.

Because of the periodicity in the horizontal directions, the dimensions of the computational box L_x and L_y must be such that the two-point correlation function of the velocity and pressure fields decays completely within half the length of the domain (see Moin & Mahesh 1998). Based on previous DNS results (Costamagna *et al.* 2003), we chose $L_x \approx 50\delta_S$ and $L_y \approx 25\delta_S$. We have carefully checked that the dimensions of the computational domain used in our simulations satisfy such a condition. The wall-normal (vertical) dimension of the domain was chosen equal to $L_z = 40\delta_S$, that is about twice the depth of the fluid column along which significant values of the Reynolds stresses are obtained, at the value of Re_δ investigated herein.

The details of the computational parameters are in table 1. Several grid resolutions were considered in the horizontal plane, all of them characterized by having uniform grid spacing. In the vertical direction the cells were clustered in the wall region using an hyperbolic tangent distribution. In particular, in most simulations about 30 cells were placed within δ_S, except case C5 where there are 60 cells, and the first velocity point from the bottom wall was located at $z^+ = 1$ (in C5 at $z^+ = 0.5$). Cases C1–C5 refer to the domain described above in conjunction with the use of a free-slip condition at the top wall and increased grid resolution.

As will be shown in the next section, in spite of the fact that grid convergence has been reached in our *quasi-dns* simulations (the definition was first given by Spalart *et al.* 1997), some disagreements between numerical results and the experimental ones have been observed, especially in the phases of the cycle where low levels of turbulence are recorded. With the aim of reducing possible sources of disagreement, two additional simulations were performed, using domain configurations different from those of cases C1–C5.

Specifically, case C6 refers to a simulation using the domain and grid spacing as in C3 together with a small-amplitude perturbation of the bottom wall. Vittori & Verzicco (1998) showed that a small-amplitude perturbation, that from a practical point of view gives a mirror-shine smooth wall, is enough to trigger turbulence in the IT regime. Vittori & Verzicco (1998) considered the following disturbance at the wall:

$$z_w(x, y) = \epsilon[\cos(0.5x) + 0.1\cos(y)]$$

with $\epsilon = h_d/\delta_S = 10^{-3}$ where h_d is the dimensional amplitude of the disturbance. We use longitudinal and spanwise wavelengths equal to those of the most unstable streamwise and spanwise modes. The first cos-function corresponds to the most unstable two-dimensional mode (Blondeaux & Seminara 1979), while according to Akhavan *et al.* (1991*b*) the second cos-function corresponds to a perturbation that gives the maximum growth rate of a three-dimensional disturbance, when

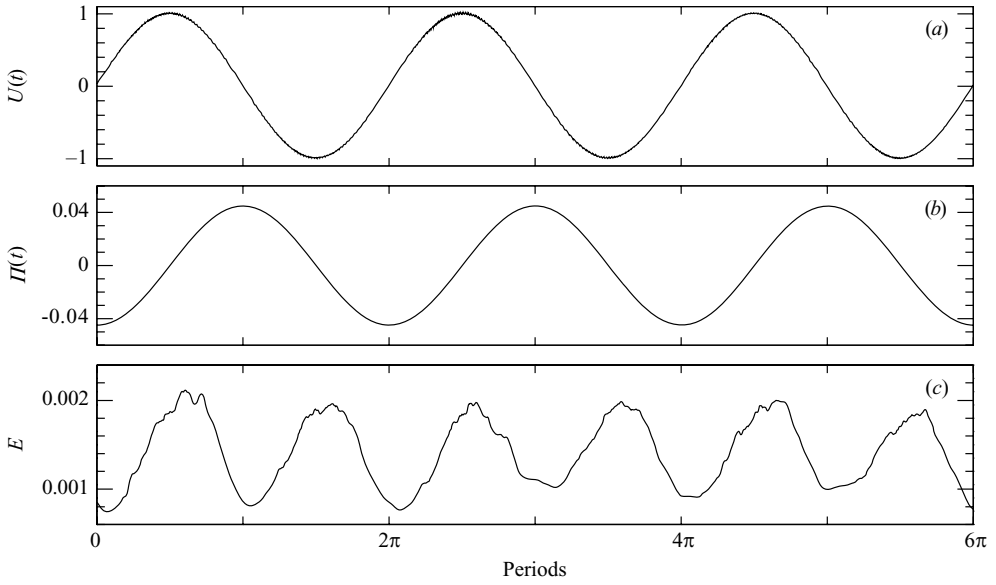

FIGURE 1. Evolution over 3 periods of simulation of relevant bulk quantities: (*a*) free-surface streamwise velocity; (*b*) driving pressure gradient; (*c*) resolved volume-integrated turbulent kinetic energy per unit volume (see (3.1)). Data from simulation C4.

superimposed on a pre-existing two-dimensional large-amplitude disturbance. The aim of simulation C6 is to show whether a small-amplitude wall perturbation may alter the level of turbulence fluctuations within the boundary layer and trigger turbulence earlier in the acceleration phases of the cycle, in order to explain possible causes of disagreement between numerical results and experimental data.

Case C7 refers to a simulation carried out with the same resolution as in C2 but using a domain delimited by two solid walls and doubled in size in the wall-normal direction, in order to check whether the free-slip condition applied at $40\,\delta_S$ could affect the turbulent statistics within the Stokes boundary layer.

Note that the non-dimensional grid spacing reported in table 1 refers to the maximum value of the wall shear stress over the cycle, hence corresponding to the minimum value of the wall unit. As will be shown in § 3 the wall shear stress at the beginning of the sharp transition to turbulence is about $(1/3)\tau_{w,max}$, thus giving a grid spacing in wall units decreased by a factor 1.7 at a phase of 30°.

Additional simulations were performed in the intermittent regime at $Re_\delta = 990$ with two main aims:

(i) to investigate the performance of the model in off-design conditions, namely in strongly non-equilibrium conditions where the hypotheses underlying the dynamic procedure cease to hold;

(ii) to compare results of a new direct simulation with available experimental data. This test was carried out to assess whether the disagreement between numerical and experimental results can be simply attributed to SGS modelling errors or needs to be sought elsewhere. The results of these tests are presented in § 4.

3. Results and discussion

Figure 1 shows, for three complete cycles of simulation, the free-stream velocity $U(t)$ as recorded at the top of the domain, the outer pressure gradient $\Pi(t)$, and the

resolved volume-integrated turbulent kinetic energy per unit volume defined as

$$E = \frac{1}{V}\int (u''^2 + v''^2 + w''^2)\,\mathrm{d}V \tag{3.1}$$

where $V = L_x L_y L_z$ is the volume of the computational box. Owing to homogeneity in the (x, y)-planes, E represents the resolved turbulent kinetic energy integrated over the depth of the fluid column per unit depth. The double prime denotes fluctuating resolved quantities, whereas we indicate with a prime the total fluctuating quantity, namely the resolved + SGS contribution.

As shown in figure 1 E varies strongly over the cycle: it starts to increase at around 30°, it peaks slightly after 90° and then decays. Such behaviour was detected in the IT regime as well by Costamagna *et al.* (2003), although in the intermittent regime they investigated the sharp increase of E occurs at the very late acceleration phases of the cycle. In their low-Reynolds-number experiment, Hino *et al.* (1983) identified two main mechanisms of turbulent production in the Stokes boundary layer: (i) a classical shear instability occurring in the mid-to-late acceleration part of the cycle, depending on the value of the Reynolds number; (ii) an explosive turbulent motion generated by the collapse of the near-wall shear occurring in the first phases of deceleration. Although the second mechanism clearly appears even in the low-Reynolds-number cases (namely in the IT regime), the first one becomes more and more important and occurs earlier in the cycle with increasing Reynolds number (see for example figure 8 of JSF89). The evolution of E over the cycle reflects this behaviour: E rapidly increases around 30°–45°, associated with the triggering to turbulence occurring at this phase due to a sudden increase of turbulent production. At the present Reynolds number ($Re_\delta = 1790$) the suppression observed by Hino *et al.* (1983) at $Re_\delta = 876$ in the late acceleration (flow state defined as *rudimentary turbulence*) is not observed, since the shear instability dominates over the favourable pressure gradient, and consequently the reduction of E in the late acceleration phase is not observed. E is maximum in the early deceleration due to the explosive-like mechanism discussed in Hino *et al.* (1983). As they report, in the mid deceleration phases E rapidly decays due to the rapid increase of turbulent dissipation related to the generation of a large population of small-scale structures (as we will show in the next section). Finally in the late deceleration phase, when the near-wall velocity reverses, a new laminar boundary layer is developing in the opposite direction, turbulent production as well as small-scale turbulent structures are almost absent, and the fluid column is characterized by the presence of large-scale structures coming from the previous phases due to a history effect. At these phases, as well as at the early acceleration phases, where the new laminar boundary layer continues to evolve, E is around its minimum, due to the residual turbulence from the preceding deceleration phases.

Figure 2 shows the non-dimensional numerical plane- and phase-averaged (already referred to as ensemble-averaged) values of the wall shear stress obtained in simulations C1–C5 together with the experimental values of JSF89, obtained using a Dantec 55R46 hot-film probe mounted in the middle of the working section. The grid C1 is not able to give an acceptable value of the wall shear stress, because the streaks are not properly resolved along the spanwise direction; as a result the maximum value of the friction coefficient

$$c_f = 2\tau_{w,max}\big/\rho U_0^2$$

is under-predicted by about 26% (0.0033 against the value $c_{f0} = 0.0044$ obtained in the experiment of JSF89). Grid C2 behaves much better (the friction coefficient is

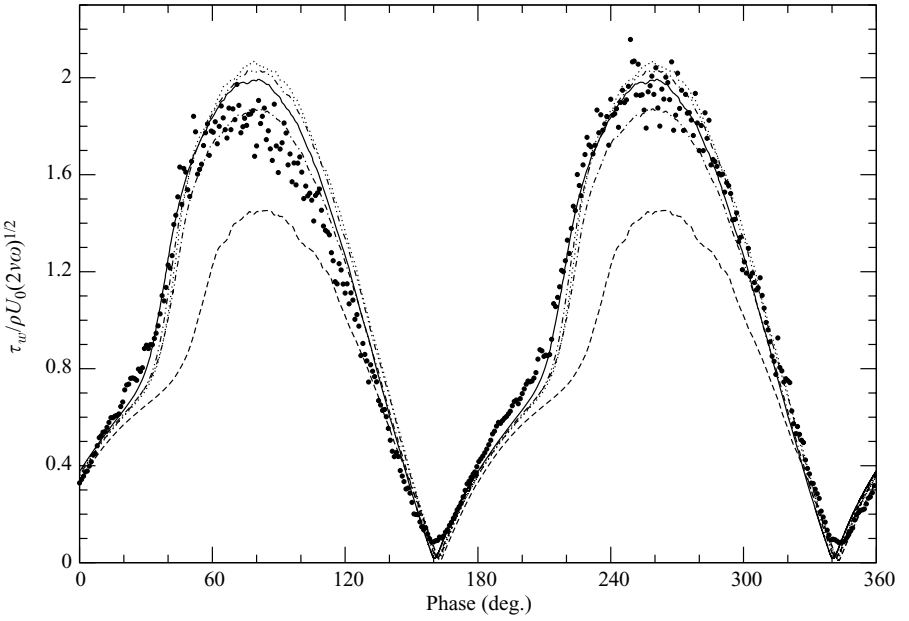

FIGURE 2. Non-dimensional wall-shear stress ensemble-averaged over 15 cycles: C1 (dashed line); C2 (dash-dotted line); C3 (dash-dot-dot line); C4 (solid line); C5 (dotted line); experimental data of JSF89 (dots).

under-predicted by 5%); however grid-convergence is obtained with grids C3, C4 and C5 which respectively give $c_f/c_{f0} = 1.03$, $c_f/c_{f0} = 1.01$ and $c_f/c_{f0} = 1.04$. The improvement obtained with grids C3–C5 compared to the results of case C2 is particularly evident during the sharp transition to turbulence observable from 30° in figure 2. Note that the streaks are well-resolved by grid C3, and a further increase of the resolution does not improve the results significantly. On the other hand, the non-dimensional grid spacing at 30° (based on the actual value of the wall shear stress at 30°) is $\Delta x^+_{30} \sim 36$, $\Delta y^+_{30} \sim 12$ and $\Delta z^+_{min,30} \sim 1.17$ with grid C3 and even smaller with the other two grids. Although in general the agreement between fine-grid results and the experimental data of JSF89 is very satisfactory, some differences are observable in figure 2, basically because the module of the ensemble-averaged wall stress obtained in the experimental tests of JSF89 appears slightly non-symmetric over a half-cycle. This feature is observable in most of the high-Reynolds-number tests of the experiments of JSF89 and, as discussed in successive work of the Danish Group (Sumer, Laursen & Fredsøe 1993; Fredsøe *et al.* 1993), can be attributed to the presence of a slight streaming that arises due to the inclusion of the rectangular working section in the U-shaped oscillatory water tunnel. On the other hand, the disagreement between numerical and experimental data in the region of near-wall flow reversal (around 160°) can be attributed to the fact that the hot-film probe is not able to give an accurate evaluation of the wall shear stress in the small time windows where the near-wall velocity is almost zero.†

† As pointed out by a referee, the experiments used the hot-film technique. The amount of heat transferred from the hot film to the fluid is constantly monitored. During the flow reversals near/at the bed, there is still heat transfer from the probe to the ambient fluid, and therefore one measures a non-zero heat conduction during these small time windows where the velocity at/near the bed is

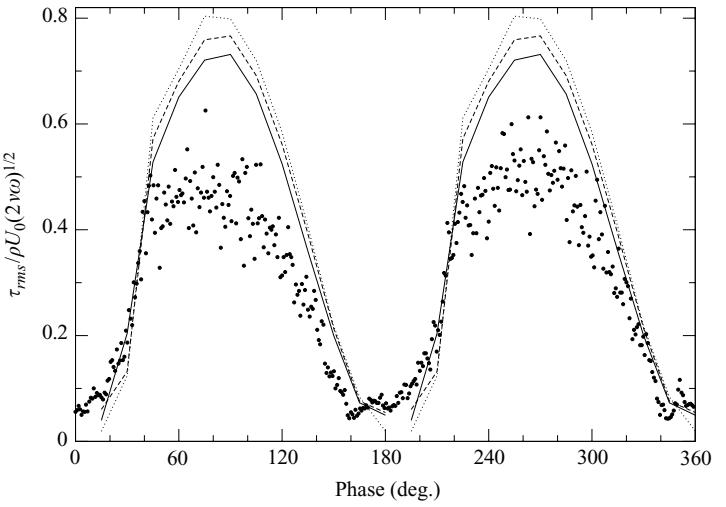

FIGURE 3. Non-dimensional r.m.s. of wall shear stress ensemble-averaged over the 15 cycles: C3 (dashed line); C4 (solid line); C5 (dotted line); experimental data of JSF89 (dots).

The evolution over the late deceleration–acceleration phases of the wall shear stress exhibits a two-slope behaviour: from 160° to about 30° for the value of Re_δ investigated herein it is characterized by a somewhat sinusoidal behaviour. This corresponds to the part of the cycle where E is around its minimum (see figure 1*c*) and a new laminar boundary layer is forming in the opposite direction with respect to the previous half-cycle. From about 30° a rapid increase of the wall shear stress is observed, that corresponds to the transition to turbulence and the rapid increase of E (see figure 1*c*). This behaviour, which is consistent with the experimental data of JSF89, is reproduced very well by our computations C3–C5. After the maximum value has been reached at about 80° the wall shear stress decays over the phases of deceleration. Again the fine-grid simulations (C3–C5) predict this behaviour very well. Consistently with JSF89, the evolution of the wall stress and of the outer velocity are not in phase (compare figure 2 with figure 1*a*). In the laminar flow case the analytical solution gives a phase delay equal to $\pi/4$; the increase of vertical mixing of momentum due to turbulence reduces the phase lag between the free-stream velocity and the wall shear stress. At $Re_\delta = 1790$, simulations C2–C5 give a phase delay of the velocity field with respect to the wall stress of around 10°, in agreement with the experiments of JSF89, whereas a somewhat smaller value (around 5°) is obtained with the coarse grid C1.

The boundary layer thickness, defined as the distance from the wall to where the mean shear is zero at 90°, is also predicted well by our simulations: C2–C5 give a value of $\delta/a \approx 0.015$ which is in fair agreement with that shown in figure 24 of JSF89 (from the experimental data the height corresponding to the maximum streamwise velocity at 90° is 23.5 mm: since $a|_{JSF89} = 1.58$ m we obtain $\delta/a|_{JSF89} = 0.0149$).

Figure 3 shows the non-dimensional ensemble-averaged r.m.s. values of the wall shear stress obtained in C3–C5, together with the data of JSF89 obtained using the single-point data of 50 oscillatory cycles. In spite of a good agreement

almost zero. So what is seen as non-zero bed shear stress is the heat measured during this time and has no physical meaning. Hence the use of raw data is erroneous for these times.

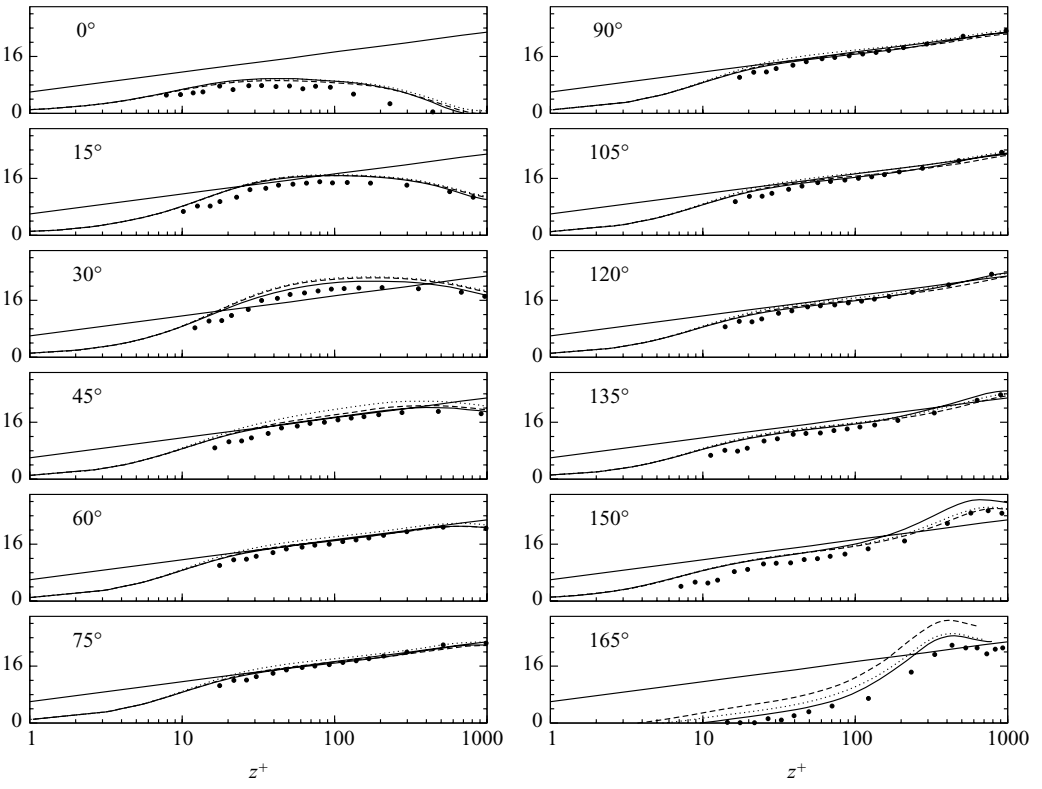

FIGURE 4. Ensemble-averaged profiles of the streamwise velocity in semi-log plot: C2 (dotted line); C3 (dashed line); C4 (solid line); C5 (dash-dotted line); experimental data of JSF89 (dots). The straight line represents the log-law with $\kappa = 0.41$ and $A = 6$.

observable during the first phases of acceleration and the late deceleration, a general overestimation is observed during the central parts of the half-cycle where fully developed turbulence is present.

Summing up, our fine-grid results (C3 to C5) reproduce very well the evolution over a cycle of the ensemble-averaged wall shear stress whereas some disagreements are observed when comparing τ_{rms} obtained in the numerical simulations with those derived from the experiments. We have checked that neither the inclusion of a small-amplitude disturbance at the bottom wall (C6), nor the use of a domain height equal to $80\delta_S$ (C7) improve the results, thus showing that the causes of such disagreement have to be sought elsewhere. Note that grid convergence was obtained in our *quasi-dns* simulations (Spalart *et al.* 1997) and appreciable variations of τ_{rms} are not expected with increased resolution. This point deserves more research.

The vertical profiles of the mean streamwise velocity, made non-dimensional with the ensemble-averaged friction velocity, are plotted every 15° in a semi-log plot in figure 4, for simulations C2–C5, together with the data from experiment 8 of JSF89. A good agreement between numerical and experimental results is observable in most of the half-cycle. Small disagreements between numerical and experimental data are observable in the range 150°–165°. This can be attributed to the fact that in this range of phases the friction velocity used for the normalization of the velocity data is very small and, consequently, small differences in this value may result in large differences in the non-dimensional velocity profiles. When making the mean velocity profiles

non-dimensional with the outer velocity U_0 (not shown) such differences disappear and the numerical data are very close to the experimental ones. Note that at 165° in figure 4 the velocity is negative close to the wall, due to the previously discussed near-wall flow reversal that has already occurred at 160° (see figure 2).

As is well known, a logarithmic vertical distribution of the mean streamwise velocity characterizes a steady boundary layer. The presence of the log-layer $u^+ = (1/\kappa)\log(z^+) + A$ was also detected in the experiments of JSF89 for the Stokes boundary layer. In particular, the authors stated: '...the higher Re, the earlier the logarithm layer comes into existence'. At $Re_\delta = 3464$ they observed a log-layer with $\kappa = 0.4$ and $A = 5$, values nearly equal to those of a canonical steady boundary layer, to span the half-cycle from about 15° to about 150°. The range of phases characterized by a log-layer becomes narrower when the Reynolds number decreases. Our results are consistent with those of the experimental investigations for test 8 at $Re_\delta = 1790$. As shown in figure 4, the presence of a log-layer is detected from about 60° to about 150°.

The values of the von Kármán constant found both for case C4 and for the experimental data, by log-fits in those phases where the log-layer is clearly observed, differ from the theoretical value of $\kappa = 0.41$ by no more than 10 % over the phases, whereas the *intercepta* A appears more sensitive to the phase position over the half-cycle. In particular, it appears to range from $A \approx 6$ for $60° < \omega t < 90°$ to $A \approx 5$ for $120° \leqslant \omega t \leqslant 150$, probably due to a low-Reynolds-number effect.

3.1. *The Reynolds stresses*

Figure 5 shows the vertical profiles of the non-dimensional Reynolds shear stress $\langle u'w' \rangle$ plotted every 15°. As previously stated, grid C1 is not able to resolve the near-wall streaks responsible for the development of $\langle u'w' \rangle$ which, as a consequence, is strongly underestimated especially at 45°, when the near-wall turbulent shear stress dramatically increases up to four times than that observable at 30°.

The general underestimation of the Reynolds shear stress in the wall region obtained with simulation C1 explains the low values of the wall stress shown in figure 2.

For the results of simulations C3–C5, the agreement between numerical and experimental data is very good, except for the last two phases characterized by a low level of the Reynolds shear stress and a general low turbulent activity (see figure 1*c*). The presence of the Reynolds shear stress is a signature of turbulent activity in wall-bounded turbulence. The analysis of figure 5 shows that such activity is particularly evident in the near-wall region and during the central phases of the cycle, from 45° to 150°, when non-zero values of $\langle u'w' \rangle$ extend along almost half the channel. On the other hand, during the initial and the final parts of the half-cycle, the Reynolds shear stress tends to be very small.

In figure 6 and 7 we show a comparison between computed and measured r.m.s. (also referred to as turbulent intensities) of the streamwise and vertical velocity components respectively. For u_{rms} our results are in good agreement with the experimental ones, especially from 30° to 105° where fully developed turbulence is observed. Apart simulation C1, no appreciable differences among the results of simulations C2–C5 are detected. Small discrepancies between numerical and experimental data are detected between 150° and 15°.

For the vertical turbulence intensity w_{rms}, generally good agreement between numerical results and experimental data is observable from 45° to 150° for simulations C3–C5. In particular, the increase of resolution in the vertical direction (grid C5) gives better agreement with experimental data in the parts of the cycle characterized by

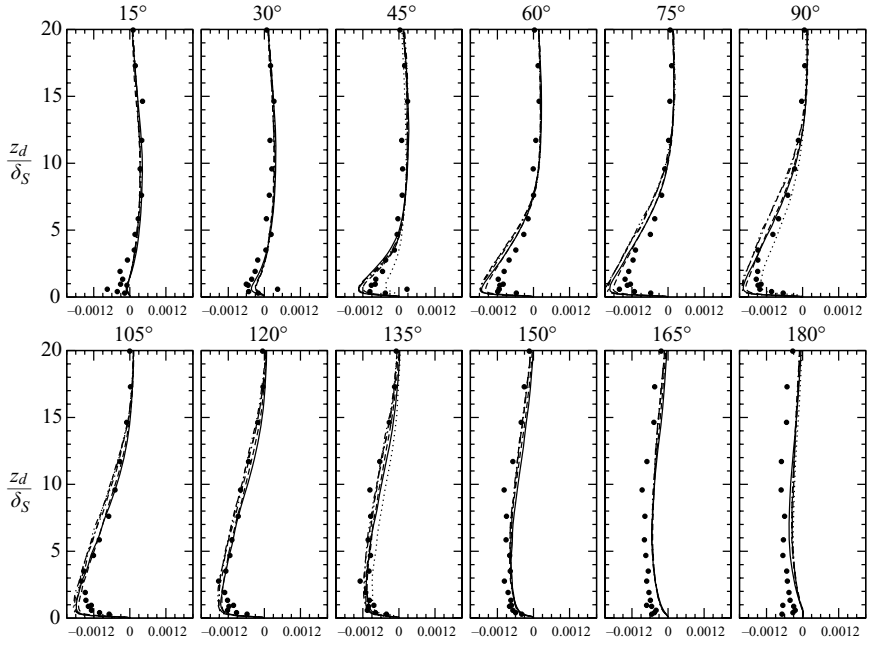

FIGURE 5. Non-dimensional ensemble-averaged Reynolds shear stress $\langle u'w' \rangle / U_0^2$ from 15° to 180°: C1 (dotted line), C2 (dashed line), C3 (dashed-dotted line), C4 (solid line), C5 (dashed-dotted-dotted line), C6 (dashed-dashed-dotted line). Dots are the experimental data of JSF89. Note that henceforth the total second-order statistics (namely resolved plus SGS part) are compared with the experimental data.

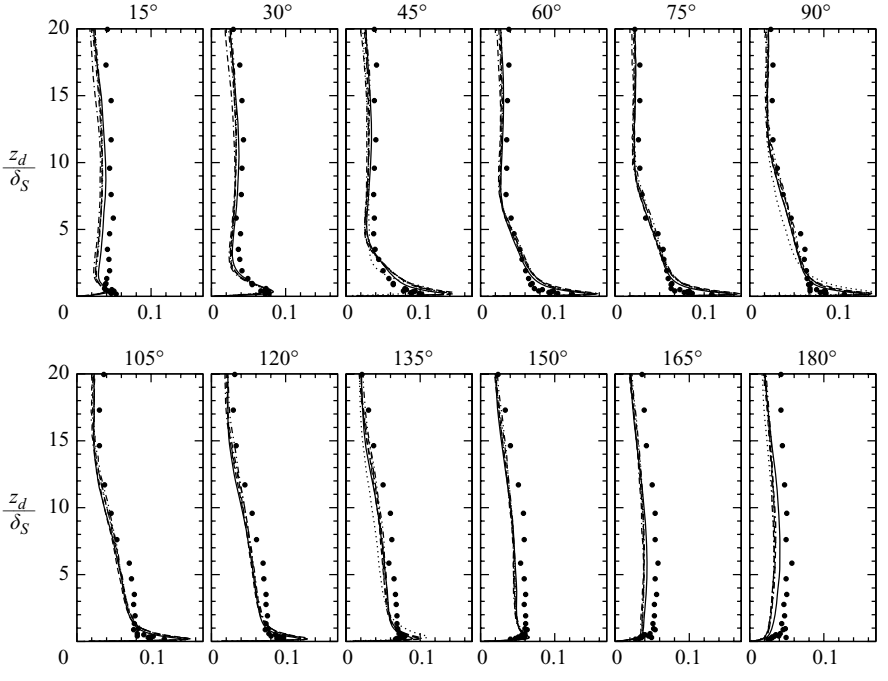

FIGURE 6. Non-dimensional streamwise turbulence intensity u_{rms}/U_0 from 15° to 180°: C1 (dotted line), C2 (dashed line), C3 (dashed-dotted line), C4 (solid line), C5 (dashed-dotted-dotted line), C6 (dashed-dashed-dotted line). Dots are the experimental data of JSF89.

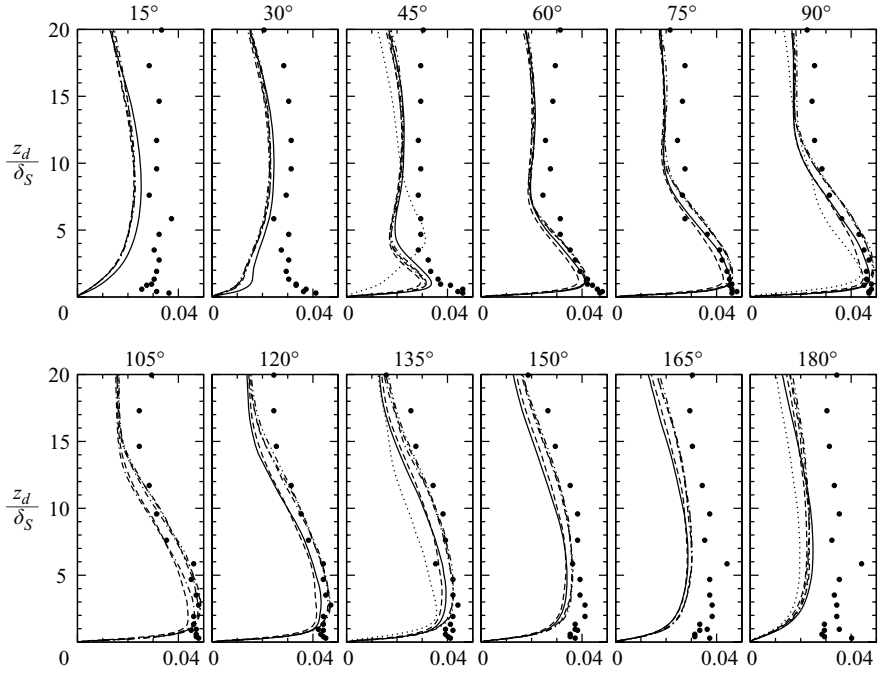

FIGURE 7. Non-dimensional vertical turbulence intensity w_{rms}/U_0 from 15° to 180°: C1 (dotted line), C2 (dashed line), C3 (dashed-dotted line), C4 (solid line), C5 (dashed-dotted-dotted line), C6 (dashed-dashed-dotted line). Dots are the experimental data of JSF89.

developed turbulence. It is noteworthy that the vertical turbulent intensity predicted with simulation C1 is qualitatively wrong at 45°, where a rapid increase of the turbulence level associated with a corresponding increase of the wall shear stress is detected.

All simulations predict values of the vertical turbulent intensity smaller than that measured by JSF89 in the range of phases between 150° and 30° where a low level of turbulent kinetic energy is recorded. Our results are in qualitative agreement with the experimental measures of Hino *et al.* (1983), who showed (in their figure 11*b*) that the vertical turbulent intensity decays by roughly a factor 2 in the late deceleration–early acceleration phases of the cycle. Note that the inclusion of a small-amplitude wall imperfection (simulation C6) does not produce appreciable variations in the results, and this is in agreement with the findings of Vittori & Verzicco (1998), who showed that beyond $Re_\delta \sim 1000$ small-amplitude wall imperfections do not affect triggering to turbulence and the level of fluctuations in the flow field. The results of grid C7 (not reported in figure 7) show that the free-surface condition applied at $z_d/\delta_S = 40$ does not affect the level of vertical fluctuations. This can be attributed to the fact that the thickness of the domain where appreciable turbulent fluctuations are observable is located below $25\delta_S$.

Finally, figure 8 shows the vertical distribution of the spanwise velocity fluctuations v_{rms}. Similarly to a canonical steady boundary layer, this quantity rapidly increases in the near-wall region, reaches its maximum where the streamwise fluctuations are large and slowly decays in the far field. For this quantity experimental data are not available, since two-dimensional measurements of the velocity field were carried out in test 8 of JSF89. However, in agreement with what was found for the other turbulent intensities, no appreciable differences were detected among simulations C3–C5.

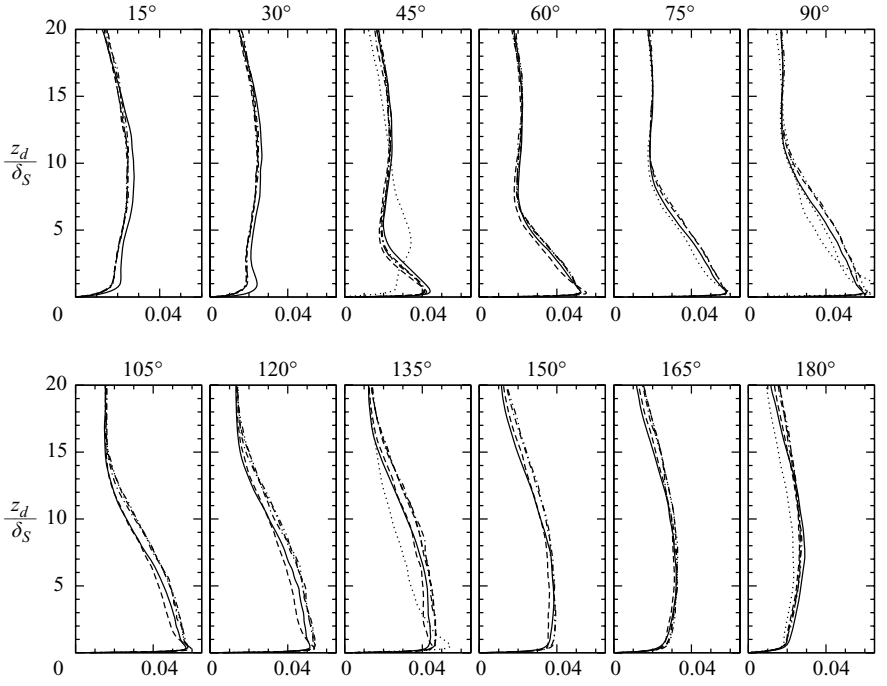

FIGURE 8. Non-dimensional spanwise turbulence intensity v_{rms}/U_0 from 15° to 180°: C1 (dotted line), C2 (dashed line), C3 (dashed-dotted line), C4 (solid line), C5 (dashed-dotted-dotted line), C6 (dashed-dashed-dotted line).

To summarize, the results of our simulations show a very good agreement between numerical and experimental Reynolds stresses, especially in the parts of the cycle where fully developed turbulence occurs. Some differences are observable for the wall-normal turbulent intensity. The magnitude of the Reynolds stresses predicted by the simulations is almost unaffected by the increased grid resolution in the phases of the cycle between 150° and 30°. This can be attributed to the fact that in those phases small-scale structures are almost absent (see Hino *et al.* 1983), so the subgrid model automatically tends to switch off, as shown in § 4, and the simulations behave similarly to a DNS.

It is difficult to speculate on the possible causes of the observed disagreements but discrepancies between numerical (DNS) results and experimental data were previously recognized in the literature, in particular in the wall-normal distribution of the ensemble-averaged Reynolds stresses. The comparison of DNS data of Spalart & Baldwin (1987) with the experimental ones of JSF89 in the IT regime ($Re_\delta = 1000$) shows some discrepancies in the ensemble-averaged Reynolds shear stress over the whole cycle, in the streamwise turbulent intensity in the central part of the cycle and in the vertical turbulent intensity in the near-wall region along the whole cycle (see figures 19–21 of JSF89). In Costamagna *et al.* (2003) discrepancies between DNS at $Re_\delta = 990$ and experimental (from JSF89, at $Re_\delta = 1000$) turbulent intensities were attributed to the fact that the numerical simulations were carried out over a small domain in all directions ($Lx/\delta_S = 25$, $L_y/\delta_S = 12.5$, $L_z/\delta_S = 25$). In § 4 we show that at $Re_\delta = 990$ disagreements between DNS and experimental data cannot be attributed to the domain size. In conclusion, our simulations show that the disagreement observed in the phases with low turbulence level is not due to:

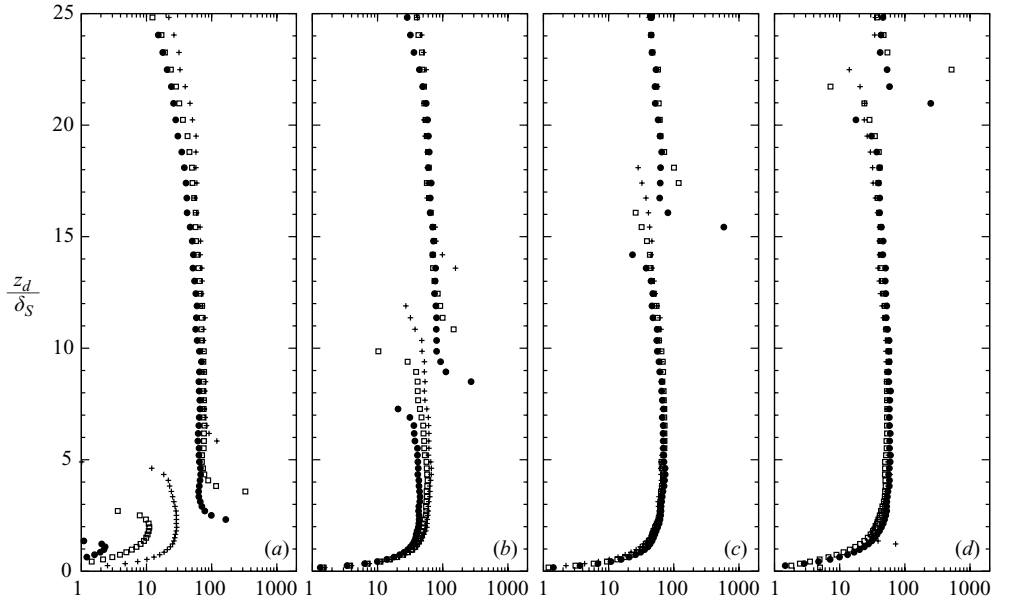

FIGURE 9. Non-dimensional eddy viscosity ν_T/ν: (*a*) 15° (●), 30° (□), 45° (+); (*b*) 60° (●), 75° (□), 90° (+); (*c*) 105° (●), 120° (□), 135° (+); (*d*) 150° (●), 165° (□), 180° (+). Data from simulation C4.

(i) the presence of the free surface at the top of the domain, when far enough from the region where significant vorticity is observed;

(ii) small-amplitude wall imperfections with wavelengths equal to those of the two-dimensional and three-dimensional most unstable modes.

However it should be pointed out that most of the disagreements are observable in the near-wall region, where, as discussed in, JSF89 p. 282, the experimental data are affected by a high drop-out rate in the laser measurements. More research is needed in order to determine the causes of the observed disagreements.

Hereafter the discussion of the characteristics of the Stokes boundary layer is based on the results of simulation C4, although no appreciable differences were observed when using data from simulations C3 and C5.

The eddy viscosity $\nu_T = -\langle u'w' \rangle / (\mathrm{d}\langle u \rangle / \mathrm{d}z)$ normalized with the molecular viscosity ν is shown in figure 9. A common feature at all the phases is the presence of a distance from the wall at which the velocity profiles have a maximum, corresponding to $\mathrm{d}\langle u \rangle / \mathrm{d}z = 0$ and thus to a singularity in the vertical distribution of the eddy viscosity. Figure 9 shows that the vertical location of the singularity monotonically increases over the half-cycle. It is interesting to observe that the eddy viscosity behaves differently in the two regions below and above the singularity. In the near-wall region, located below the singularity point, from 0° to 45° the eddy viscosity is very small and rapidly increases from $O(1)$ to $O(10)$. This corresponds to the presence of the rapidly evolving near-wall laminar boundary layer. In the remaining half-cycle the near-wall region is characterized by $\nu_T/\nu \sim O(10^2)$. Conversely, the outer region (above the singularity point) is characterized by having a nearly constant eddy viscosity $O(10^2)\nu$ over the whole half-cycle. In particular, we observe the presence of relevant eddy viscosity up to $z_d/\delta_S \sim 25$, well above the singularity point, that, according to the canonical definitions of boundary layer theory, would characterize the thickness of

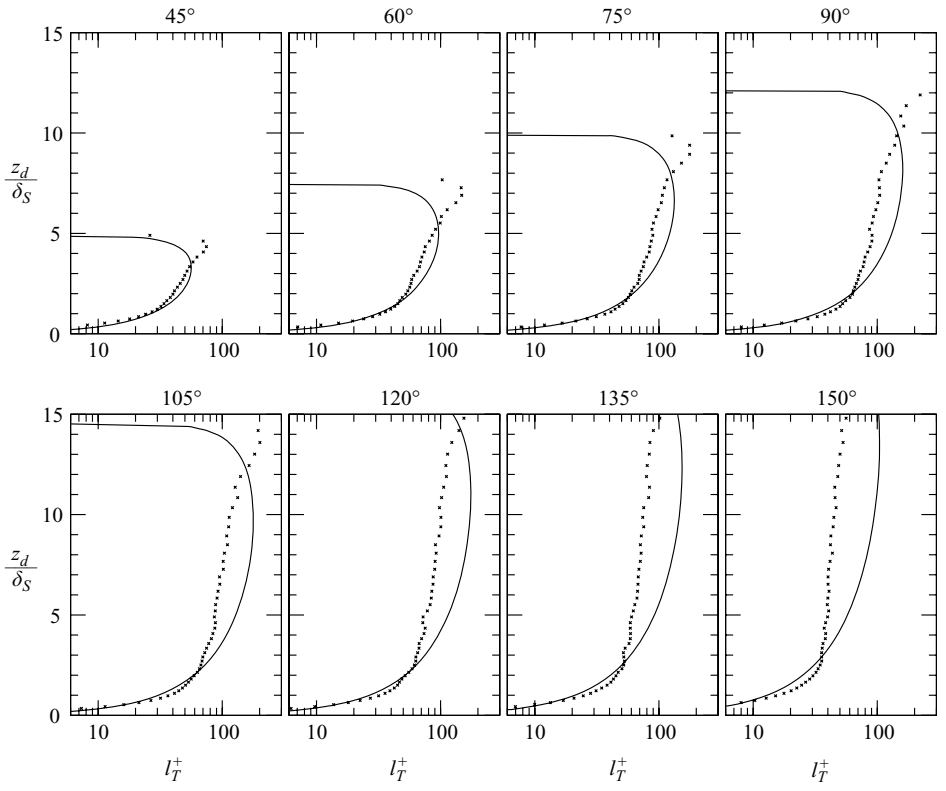

FIGURE 10. Evolution of the mixing length from 60° to 135°. The crosses are the value calculated from (3.2) in conjunction with data from C4. The solid line is the theoretical expression given by (3.3). The quantity is made non-dimensional with the wall unit z^* calculated at each phase using the ensemble-averaged value of the friction velocity.

the oscillating boundary layer. The presence of relevant eddy viscosity above the boundary layer thickness is due to a history effect (Hino *et al.* 1983; JSF89), namely large-scale turbulent structures generated in previous phases of the half-cycle tend to remain in the flow field during the late deceleration where turbulent production has ceased. At $z_d/\delta_S > 25$ turbulence activity is not detected and the flow field appears irrotational.

The concept of mixing length is closely related to eddy viscosity and the existence of the log-layer previously discussed. We have evaluated the mixing length l_T using the classical expression, as also reported in Pope (2000),

$$\nu_T = l_T^2(\mathrm{d}\langle u\rangle/\mathrm{d}z), \tag{3.2}$$

for those phases where a well-developed log-layer clearly appears. In figure 10 we plot l_T calculated from the data of simulation C4, and compare it with the theoretical value

$$l_{T,th} = \kappa z\sqrt{1 - z/D} \tag{3.3}$$

where D is the distance from the wall at which $\langle u'w'\rangle$ goes to zero, and $\kappa = 0.41$. The theoretical value assumes $\langle u'w'\rangle$ to be a linear function of z and the presence of a logarithm velocity profile. The mixing length, expressed in wall units, increases from an average value of about 80 at 60° up to about 100 between 105° and 120°, then decreasing to around 80 at 135°. Since the mixing length is a rough measure

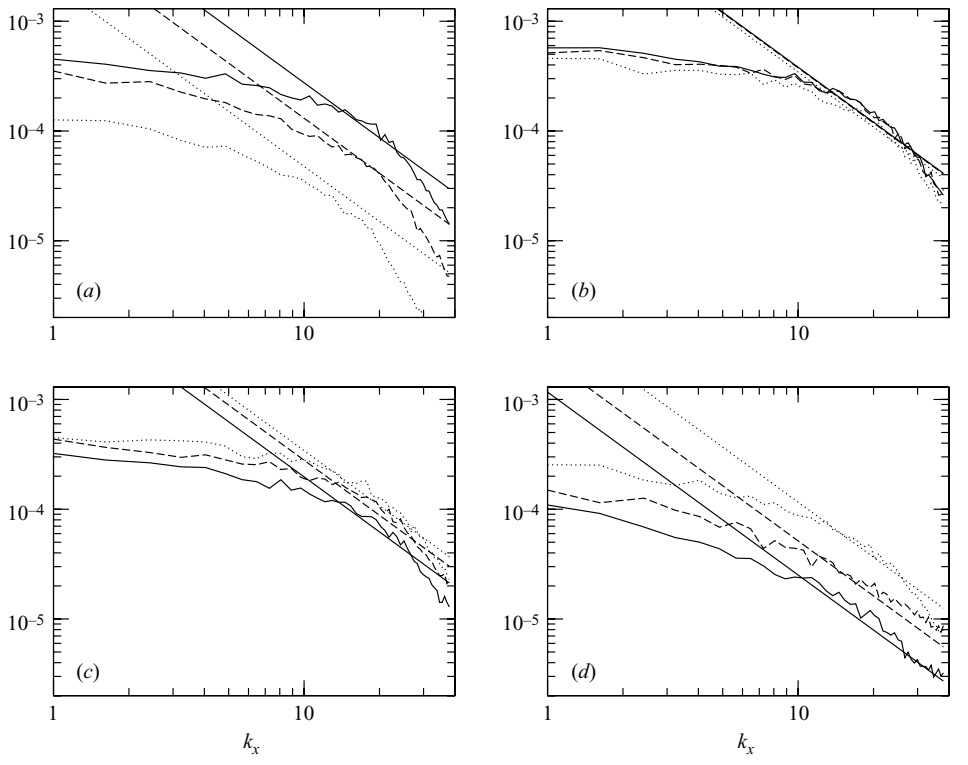

FIGURE 11. Spectra of resolved streamwise fluctuation E_{11}/U_0^2 along the streamwise direction, at $z_d = \delta_S$: (*a*) 15° (dotted line), 30° (dashed line), 45°(solid line); (*b*) 60° (dotted line), 75° (dashed line), 90° (solid line); (*c*) 105° (dotted line), 120° (dashed line), 135° (solid line); (*d*) 150° (dotted line), 165° (dashed line), 180° (solid line). The straight lines are the isotropic Kolmogorov spectra $(18/55)C_s\epsilon^{2/3}k^{-5/3}$ with the dissipation rate ϵ calculated at the actual phases; $C_s = 1.5$ is the universal Kolmogorov constant (Sreenivasan 1995). Data from simulation C4.

of the extent of the largest eddies present in the flow field, we observe that, once the log-layer is established in the cycle, the vertical scale of these eddies increases up to a maximum value which is about 1/30 of the entire channel height and about 120 % of the thickness of the laminar Stokes boundary layer. The small departures from the theoretical value observable in the outer region are due to the fact that in this region the mean shear $\mathrm{d}\langle u\rangle/\mathrm{d}z$ slightly deviates from the theoretical value $u_\tau/\kappa z$.

3.2. *The turbulence structure*

Figures 11, 12, 13 show the one-dimensional spectra of resolved velocity fluctuations along the x-direction at $z_d = \delta_S$. Figures 11 and 13 also contain the universal Kolmogorov spectra:

$$E_{11} = \frac{18}{55}C_s\epsilon^{2/3}k^{-5/3}, \qquad E_{33} = \frac{24}{55}C_s\epsilon^{2/3}k^{-5/3},$$

with $C_s = 1.5$ (see Sreenivasan 1995) that hold for equilibrium turbulence in the limit of high-Reynolds-number flow.

In the initial phases of the acceleration part of the half-cycle (around 15°), figure 11(*a*) shows that the level of the turbulent fluctuations in the direction of motion is very small. Interestingly, at this phase the spectrum of the spanwise turbulent fluctuations E_{22}/U_0^2 (figure 12*a*) has the same order of magnitude as E_{11}/U_0^2, whereas

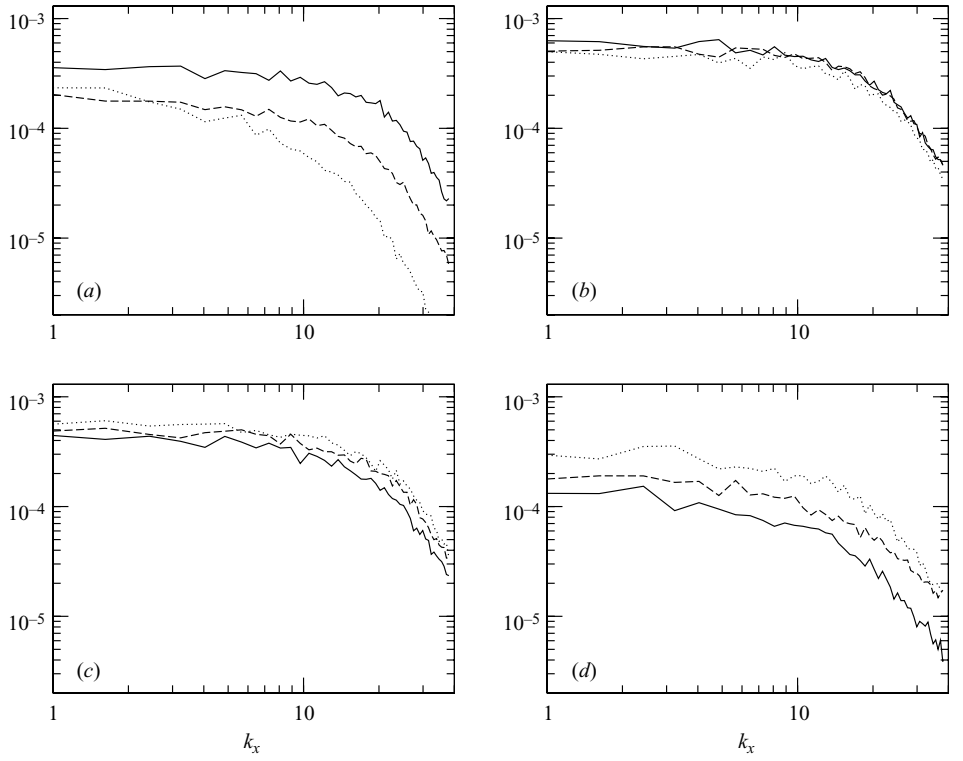

FIGURE 12. Spectra of resolved spanwise fluctuation E_{22}/U_0^2 along the streamwise direction, at $z_d = \delta_S$: (*a*) 15° (dotted line), 30° (dashed line), 45°(solid line); (*b*) 60° (dotted line), 75° (dashed line), 90° (solid line); (*c*) 105° (dotted line), 120° (dashed line), 135° (solid line); (*d*) 150° (dotted line), 165° (dashed line), 180° (solid line). Data from simulation C4.

the spectrum of vertical turbulent fluctuations is about one order of magnitude smaller than that of the other two components (figure 13*a*). In other words, as will be also shown later, at this phase turbulence is much more energetic in the horizontal planes than in the vertical direction. As the phase of motion increases (figures 11*a*, 12*a*, 13*a*) the overall level of energy increases in the direction of the motion as well as in the vertical direction over the whole range of wavenumbers, thus indicating that the rapid growth of turbulence occurs through interaction between streamwise and vertical motion. When the phase ranges between 45° and 105° (figures 11*a–c*, 12*a–c*, 13*a–c*) the level of energy remains nearly constant and the presence of a short inertial subrange having a canonical slope $k^{-5/3}$ is detected (as also observed in the experimental study of Hino *et al.* 1983). Although the inertial subrange appears very short, at these phases the spectra of E_{11} and of E_{33} fit the Kolmogorov universal law. During the mid-deceleration, equilibrium conditions are progressively lost and the energy spectra depart from the universal law. This is in agreement with the findings of Hino *et al.* (1983) who observed that due to a pronounced energy dissipation occurring at mid-deceleration the spectra appear to depart from the $k^{-5/3}$ law. In the late phases of the deceleration the level of the resolved turbulent fluctuations decreases at all scales (figures 11*d*, 12*d*, 13*d*), but, similarly to the behaviour observed at 15°, the vertical fluctuations decay much more rapidly than the other components. From 150° to 30°, an inertial range cannot be detected (figures. 13*d* and 13*a*) and the value of the constant C_s changes from phase to phase, thus showing lack of universality.

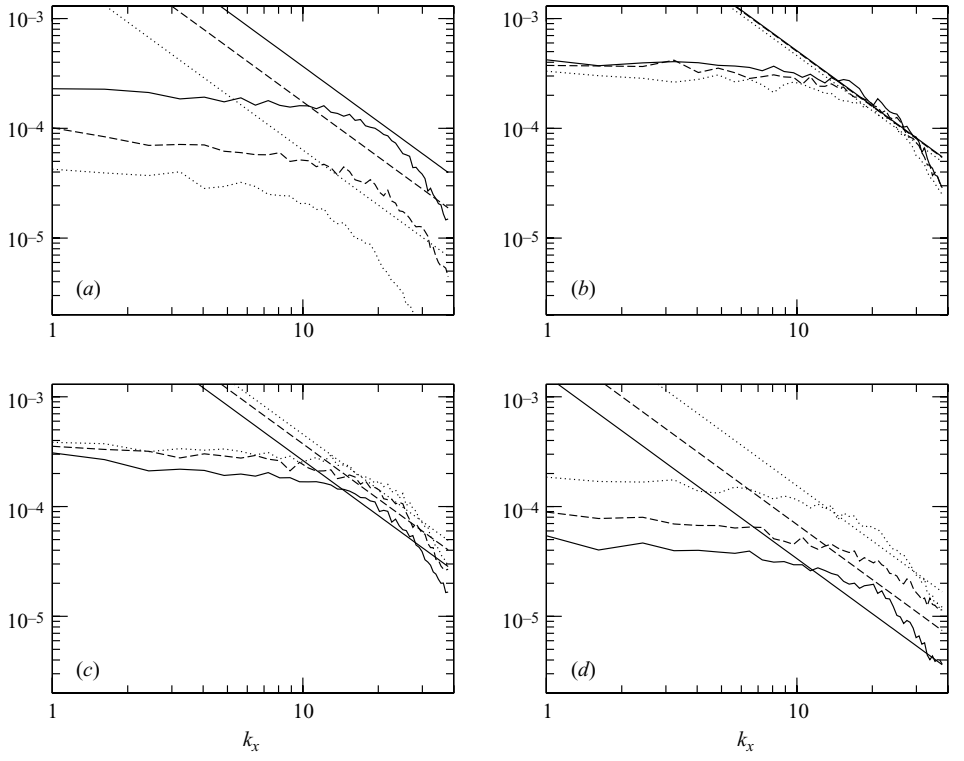

FIGURE 13. Spectra of resolved vertical fluctuation E_{33}/U_0^2 along the streamwise direction, at $z_d = \delta_S$: (*a*) 15° (dotted line), 30° (dashed line), 45°(solid line); (*b*) 60° (dotted line), 75° (dashed line), 90° (solid line); (*c*) 105° (dotted line), 120° (dashed line), 135° (solid line); (*d*) 150° (dotted line), 165° (dashed line), 180° (solid line). The straight lines are the isotropic Kolmogorov spectra $(24/55)C_s\epsilon^{2/3}k^{-5/3}$, with the dissipation rate ϵ calculated at the actual phases; $C_s = 1.5$ is the universal Kolmogorov constant (Sreenivasan 1995). Data from simulation C4.

This effect can be attributed to the fact that from 150° to 30° the flow field is in non-equilibrium conditions. Specifically, as first showed by Hino *et al.* (1983), the late deceleration is characterized by absence of near-wall turbulent production due to the rise of a new laminar boundary layer in the reverse direction, and the flow field contains large eddies accompanied by few small-scale structures; the early acceleration is characterized by the growth of the laminar boundary layer and the few structures present in the flow field are residual ones generated during the preceding deceleration phases.

An effective way to quantify departure from equilibrium is to compute the structure parameter $a_1 = \langle u'w' \rangle / 2K$ where $K = 1/2 \ \langle u_i' u_i' \rangle$ is the turbulent kinetic energy. For steady turbulence, $a_1 \approx 0.15$ in the logarithmic layer, whereas lower values are typical of three-dimensional boundary layer and non-equilibrium flows. The structure parameter a_1 was used by, among others, Scotti & Piomelli (2001) in the pulsating flow case to characterize the phases of the oscillatory cycle. In figure 14 we show the evolution of the structure parameter over a half-cycle. In the early acceleration (15° to 30°) the structure parameter is noticeably smaller than 0.15 in the whole fluid column; from 60° to 150° a plateau is reached in the log-region, with a value slightly larger than 0.15, thus revealing the presence of equilibrium turbulence. Later

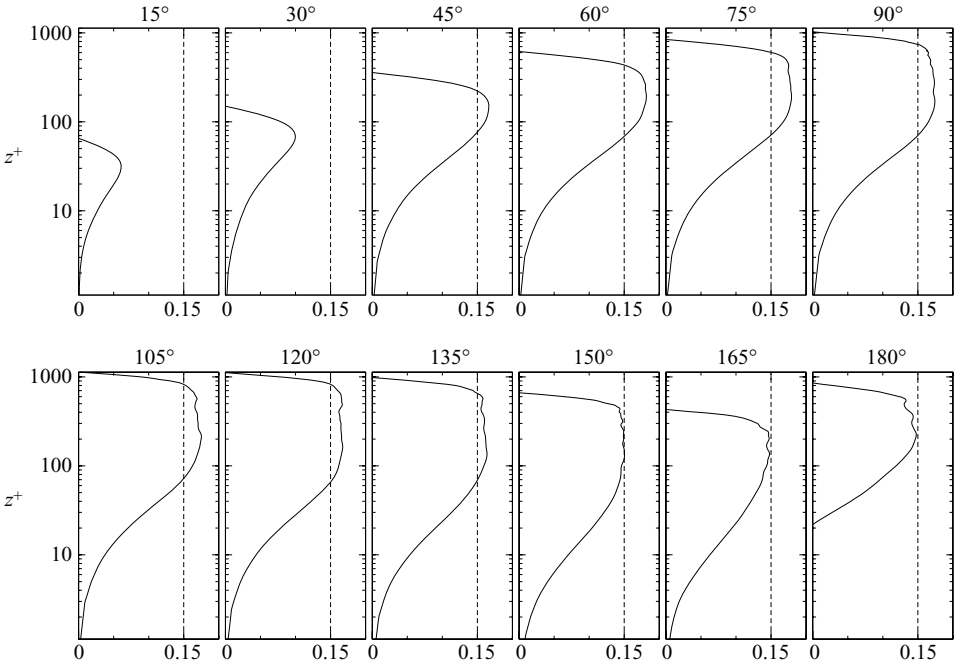

FIGURE 14. Structure parameter a_1 in semi-log plot from 15° to 180°. Data from simulation C4.

the presence of a plateau is no longer detected and a_1 progressively decreases, thus showing departure from equilibrium occurring in the late deceleration.

In order to get a picture of the mechanism by which turbulent energy is generated and dissipated over the oscillation, in figure 15 we show the evolution of the mean production and dissipation rates of the resolved turbulent kinetic energy throughout the half-cycle:

$$P_K = -\langle u''w''\rangle \frac{\mathrm{d}\langle u\rangle}{\mathrm{d}z} - \langle \tau_{13}\rangle \frac{\mathrm{d}\langle u\rangle}{\mathrm{d}z}, \tag{3.4}$$

$$\epsilon_K = -\frac{1}{Re}\left\langle \frac{\partial u_i''}{\partial x_j}\frac{\partial u_i''}{\partial x_j}\right\rangle - \langle \tau_{ij}S_{ij}\rangle. \tag{3.5}$$

Figure 15 shows that both production and dissipation of turbulent kinetic energy switch on between 30° and 45° and, from 45° to 120° their vertical distribution resembles that of a canonical steady boundary layer. On the other hand, over the half-cycle, both terms strongly decrease up to a complete suppression observable from 165° to the end of the half-cycle. This suppression is related to the inversion of the velocity profile in the near-wall region and the early developing of a laminar boundary layer in the reverse direction. The maxima of production rate are very close to the wall, located approximately at $0.14\delta_S$ between 60° and 120° that, in wall units, corresponds to $z^+ \approx 11$–12, thus being within the buffer layer. The maximum values of the non-dimensional production rate and dissipation rate, respectively 0.22 and −0.16, are close to the values obtained for the canonical steady plane-channel flow at a friction Reynolds number equal to 180 (Mansour, Kim & Moin 1988), respectively equal to 0.21 and to −0.166. This suggests that once a fully developed turbulent state

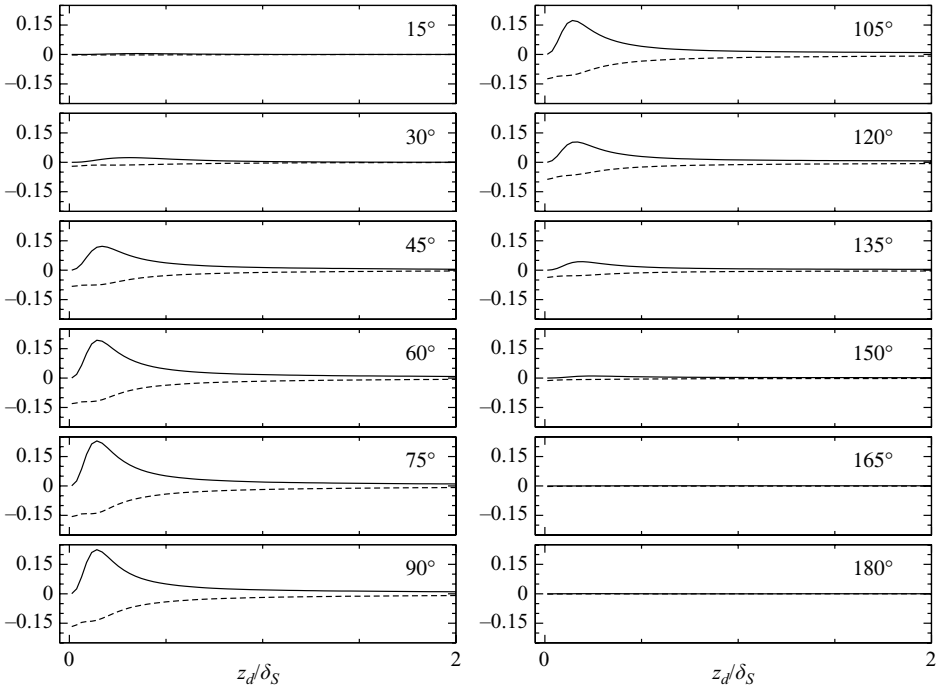

FIGURE 15. Vertical profiles of production rate (solid line) and dissipation rate (dashed line) of the resolved turbulent kinetic energy from 15° to 180°. The quantities are made non-dimensional with $u^4_{\tau,max}/\nu$. Data from simulation C4.

has been reached, the Stokes boundary layer evolves along a series of quasi-steady equilibrium turbulent states.

The evolution over a half-cycle of the vertically integrated terms per unit depth (henceforth referred to as *specific*) that contribute to the resolved turbulent kinetic energy is shown in figure 16. We have also plotted the specific numerical dissipation rate, which is associated with the use of second-order-accurate numerical schemes. This quantity is calculated by difference among all the terms composing the budget of the specific turbulent kinetic energy. The specific production rate as well as the specific overall dissipation rate (the sum of the molecular, SGS and numerical ones) sharply increase beyond 30°. At 45° values more than three times larger than those at 30° are observed. The specific production as well as the specific overall dissipation rate have their maxima around 90° and then they gradually decrease over the deceleration phases of the cycle. The unsteady term is always much smaller than the others but still visible in the plot. The smallness of the time-dependent term is related to the fact that in most of the cycle of oscillation the turbulent field is in quasi-equilibrium conditions as previously discussed. Figure 16 shows that the unsteady term is positive in the acceleration phases of the cycle where K rapidly increases, it is nearly zero in the central phases of the cycle where turbulence is in equilibrium conditions and finally it is negative when turbulence decays, namely in the late deceleration phases. The specific numerical dissipation rate is always much smaller than the overall specific dissipation rate and also smaller than that given by the SGS model.

Most experimental and numerical studies aimed at the identification and interpretation of the coherent structures have dealt with steady wall-bounded flows (for a review see Robinson 1991). Recently, the evolution of turbulent coherent structures

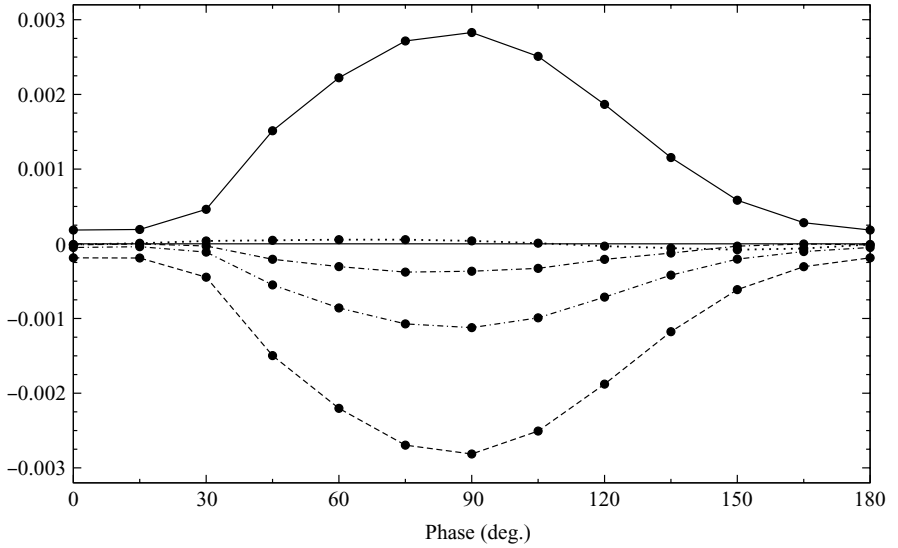

FIGURE 16. Balance of the resolved turbulent kinetic energy over a half-period: specific production rate, solid line; specific SGS dissipation rate, dashed-dotted line; specific numerical dissipation rate, dashed-dashed-dotted line; specific overall dissipation rate (*molecular* + *SGS* + *numerical*), dashed line; specific unsteady term, dotted line. All quantities are made non-dimensional with $u_{\tau,max}^4/\nu$. The zero line is also plotted for clarity. Data from simulation C4.

in a Stokes boundary layer has been investigated experimentally by Sarpkaya (1993) and by Costamagna *et al.* (2003) by means of direct numerical simulation. Both investigations were carried out in the IT regime.

In particular, in the experimental study of Sarpkaya (1993) at $Re_\delta \approx 400$ irregularly spaced low-speed streaks were observed between the final decelerating phases and the early accelerating ones, where they completely disappear. At $Re_\delta \approx 420$–460, these streaks begin to interact with each other, giving rise to quasi-coherent structures. At these values of Re_δ vortical structures eventually start to emerge. They increase in number and tend to merge into a single streak, which, after having became sinuous, breaks into shorter segments which grow in amplitude giving rise to heart-shaped small structures during the deceleration.

The numerical investigation of Costamagna *et al.* (2003) in the IT regime at $Re_\delta = 800$ showed that the generation of longitudinal equi-spaced streaks appears around the end of the acceleration phase of the cycle and that their break-up always occurs during the deceleration phase of the cycle.

Figure 17 shows contour plots of the streamwise resolved velocity fluctuations u'' on a plane at $z^+ = 7$ over a half-cycle. Consistently with the above investigations, narrow longitudinal streaks initially appear in the flow field (at 15° in the present case), and appear well-developed and equi-spaced along the y-direction at 30°. Later (at 45°) they rapidly coalesce into single more energetic structures and finally they break into small structures. The presence of a large population of such small structures is evident from 60° (late acceleration part) to 150° (deceleration part). Then, the observed structures tend to decay in intensity and at the same time to lose their elongated shape (up to 180°). In the late acceleration phase, in agreement with the findings of Hino *et al.* (1983), few large-scale structures are observable in the near-wall region. A qualitative comparison of the present results obtained in the turbulent

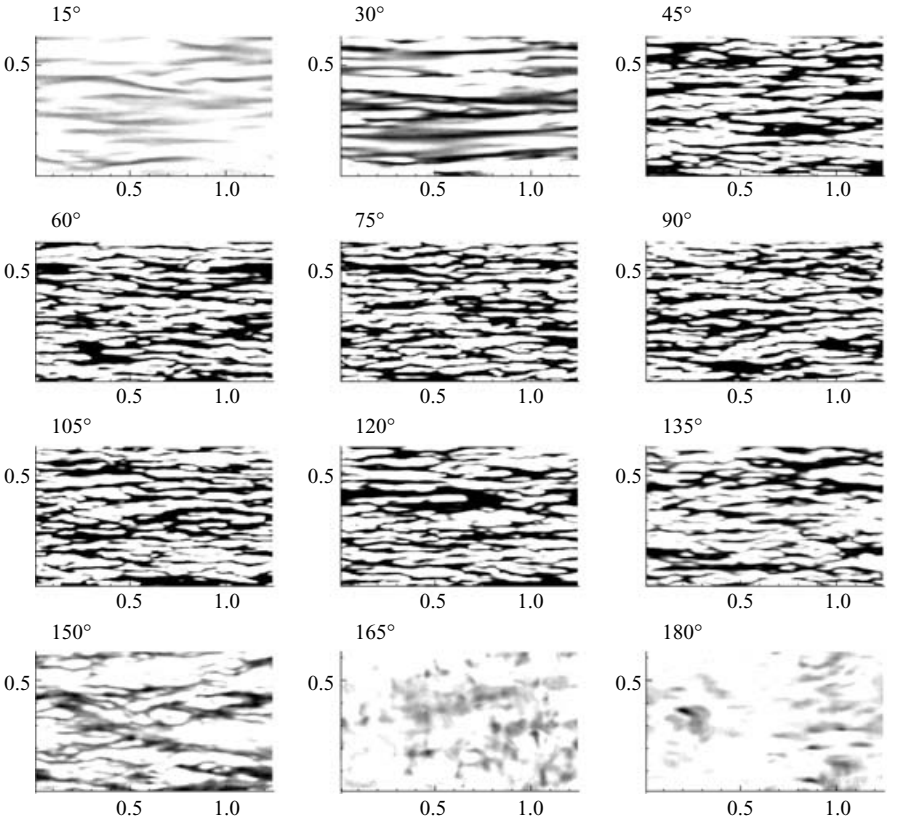

FIGURE 17. Contour plots of the fluctuating streamwise velocity u'' with respect to the plane-averaged throughout a half-cycle at $z^+ = 7$ calculated using $z^* = \nu/u_{\tau,max}$. Regions with negative values are depicted in scales of grey. Data from simulation C4.

regime ($Re_\delta = 1790$), with those of Sarpkaya (1993) at $Re_\delta \sim 420$–460, of Costamagna *et al.* (2003) at $Re_\delta = 800$ in the intermittent turbulent regime, and of Scotti & Piomelli (2001) for pulsating flow in the low-frequency regime under conditions characterized by periodic relaminarization and re-transition to turbulence (see their figure 22 for a simulation at $Re_s = 500$, where Re_s is the Reynolds number based on the Stokes thickness and the amplitude of velocity of the oscillatory component of the motion), shows that the genesis and evolution of the near-wall streaks is nearly independent of the flow regime. The presence of elongated equi-spaced streaks, their coalescence and their successive destruction into a large population of smaller energetic structures seems to be a common feature of the four investigations. On the other hand, the phases in the half-cycle along which the streaks develop, evolve and eventually break into small structures, are strongly dependent on the value of the Reynolds number. An analysis of our results compared to those of Sarpkaya (1993) and Costamagna *et al.* (2003), suggests that the formation of the elongated equi-spaced streaks is shifted back over the half-cycle toward the phases of acceleration and that the break-up of these structures does not necessarily occur over the deceleration phases, as suggested by Costamagna *et al.* (2003). In fact, we observe this break-up to occur at a phase angle approximately between 45° and 60°, well before the beginning of the deceleration phases. This finding is in agreement with the analysis of JSF89,

who observed the rise of turbulence earlier in the cycle with increasing values of the Reynolds number. Similar qualitative behaviour has also been observed by Lohmann *et al.* (2006).

It is well-known (Pope 2000) that in a canonical boundary layer the spacing between the streaks in the near-wall region ($z^+ < 7$) is distributed between about 80 and 120 wall units, independent on the Reynolds number. Their length in the streamwise direction can be as large as more than 1000 wall units, and their width is around 100 wall units. In our simulations the mean spacing between two streaks calculated at a distance $z^+ = 7$ from the wall at phase of 30°, when the coherent structures are clearly observed, is around 110 wall units, which is within this range. This value is in good agreement with that observed by Sarpkaya (1993) (between 85 and 135 wall units at $Re_\delta = 420$–460) and also with the average streak spacing of 127 calculated by Costamagna *et al.* (2003) ($Re_\delta = 800$) at a distance of about $z^+ = 8$ from the wall.

As argued by Sarpkaya (1993), according to the steady channel flow analysis of Lam & Banerjee (1992), there exists a critical value of the shear Reynolds number $Re(crit)^* = u_\tau \delta_S / \nu = (\sqrt{2} Re_\delta)^{1/2}$ ranging from 20 to 28 below which the near-wall elongated streaks disappear. An average value of $Re(crit)^* \approx 24$ gives $Re_\delta \approx 400$, which corresponds to the threshold at which the streaks appear and disappear periodically in Sarpkaya's experiments. Our $Re_\delta = 1790$ yields $Re^* \approx 50$, which is larger than the critical value found by Lam & Banerjee (1992) for steady currents. However, if we apply the $Re(crit)^*$ criterion of Lam & Banerjee (1992) using the ensemble-averaged values of the friction velocity evaluated at each phase during the oscillation we observe that only in the range 150°–180° are values of Re^* of the order of 30 (near the threshold given by Lam & Banerjee 1992) recorded, whereas, in the remaining part of the half-cycle Re^* ranges from 40 to 80. On the other hand, as observed in figure 17, the presence of clear elongated structures can be detected from about 15° up to 150°, in the range of phase angles at which Re^* is well above the critical value. This suggests that, though Sarpkaya (1993) noted as *fortuitous* the agreement of his results with the criterion of Lam & Banerjee (1992), our results support his intuition. Indeed, we observe that a such a criterion may hold in the case of an oscillating boundary layer, provided that the shear Reynolds number is calculated at each phase using the ensemble-averaged value of the friction velocity.

A very effective way to visualize the vortical structures in the turbulent field is the Q-criterion (Dubief & Delcayre 2000). This criterion was also employed by Scotti & Piomelli (2001) for the visualization of turbulent coherent structures in the pulsating boundary layer case. Q is the second invariant of the velocity gradient tensor $\nabla \mathbf{u}$ and is defined as

$$Q = \frac{1}{2}(\overline{\Omega}_{ij}\,\overline{\Omega}_{ij} - \overline{S}_{ij}\,\overline{S}_{ij}) = -\frac{1}{2}\frac{\partial \overline{u}_i}{\partial x_j}\frac{\partial \overline{u}_j}{\partial x_i}, \tag{3.6}$$

where $\overline{\Omega}_{ij}$ and $\overline{S}_{ij}$ are respectively the antisymmetric and the symmetric components of the resolved velocity gradient tensor. The condition $Q > 0$ has been found to be effective in the identification of regions characterized by the presence of coherent vorticity (Hunt *et al.* 1988). Figure 18 shows the evolution of the isosurfaces $Q/Q_0 = 0.2$ (with $Q_0 = U_0^2/a^2$) from 45° to 150° obtained using the same instantaneous field as in figure 17. Rotational motion is very weak ($Q/Q_0 < 0.2$) during the early acceleration where the new near-wall laminar boundary layer is developing; significant large-scale vorticity develops around 45°, during the sharp transition to turbulence. In the mid-to-late acceleration part of the cycle (figure 18*b–d*) elongated vortical

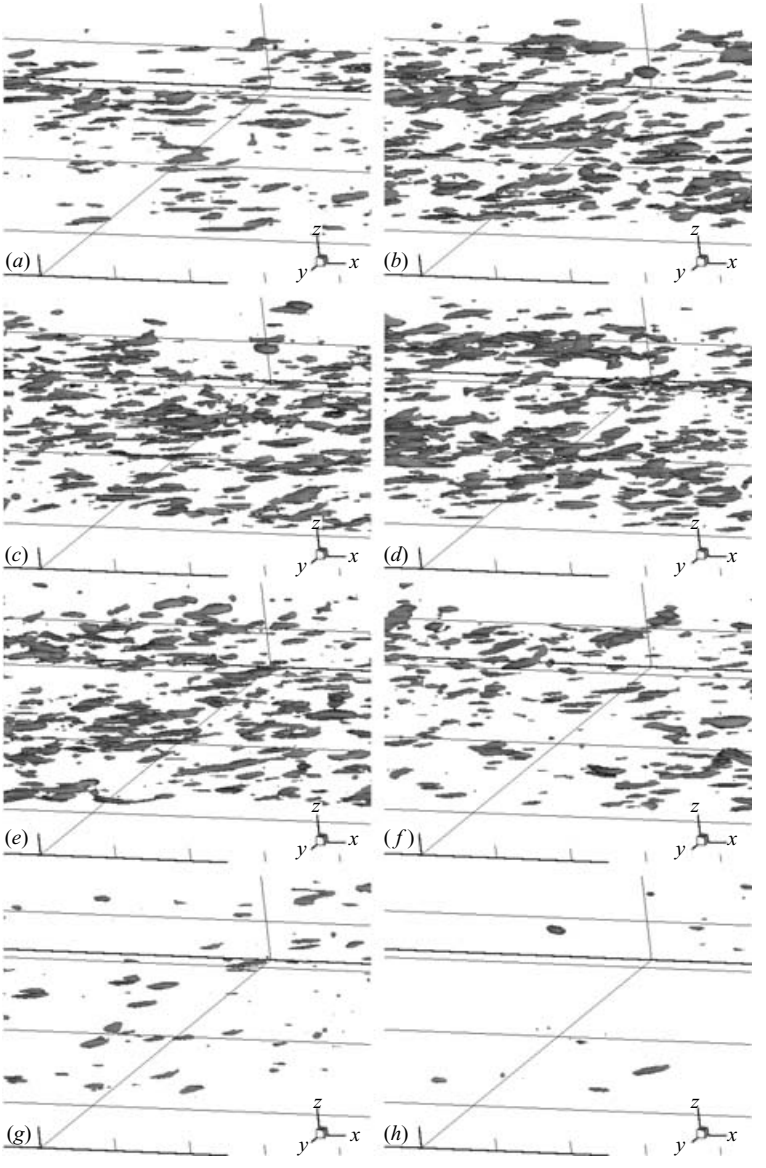

FIGURE 18. Isosurfaces of Q in the wall region in the following phases: (*a*) 45°, (*b*) 60°, (*c*) 75°, (*d*) 90°, (*e*) 105°, (*f*) 120°, (*g*) 135°, (*h*) 150°. The value $Q/Q_0 = 0.2$ is visualized (data from simulation C4). The direction of the main flow is from left to right.

structures inclined upward are observable. The vortical structures visualized using Q increase in number and, at the same time, decrease in size, still remaining oriented along the streamwise direction and inclined upward, over the half-cycle. Similar structures were also observed by Scotti & Piomelli (2001) in the pulsating flow in the current-dominated low-frequency regime, when cyclic relaminarization and re-transition to turbulence occur (see their figure 22). Once the break-up of the initial long streaks has occurred (between 45° and 60°, figure 18*b*, *c*), a large population of elongated short vortical structures is present in the flow field and their number and intensity gradually decrease over the deceleration phases of the half-cycle (figure 18*g*, *h*).

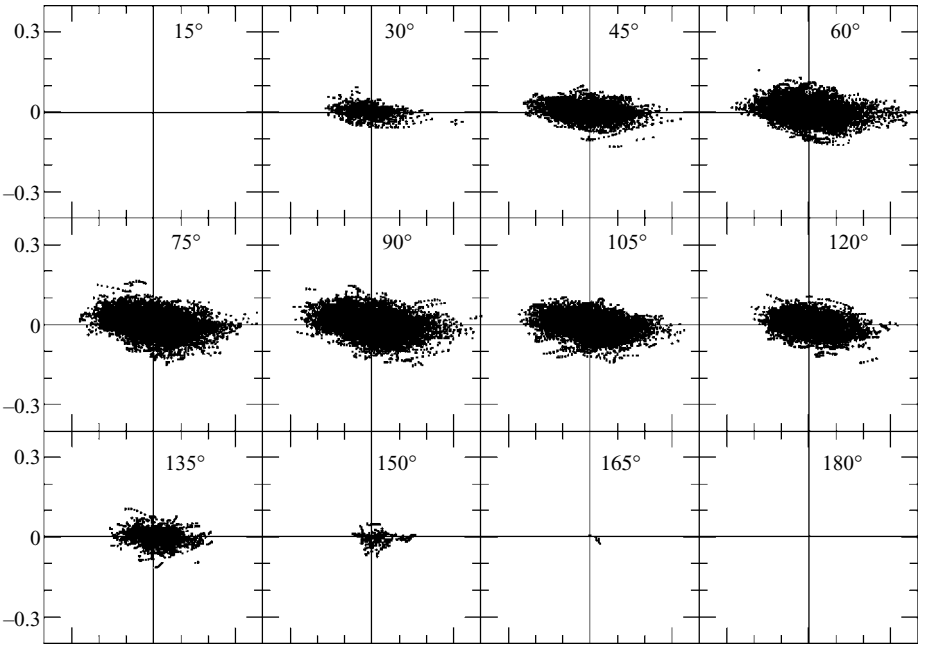

FIGURE 19. u'' and w'' sample space conditioned to $Q/Q_0 > 0.15$. The horizontal axis is u''. Data from simulation C4.

The effect of these structures on the turbulent characteristics of the flow field can be analysed by means of the quadrant analysis of Wallace, Eckelmann & Brodkey (1972). In figure 19 we plot, for each phase, the u–w sample space of the resolved fluctuations using the fields shown in figure 18. The II and IV quadrants are respectively representative of ejection and sweep events whereas the other two quadrants are not representative of turbulent structures (see Pope 2000 for a detailed description). The u''–w'' values plotted in figure 19 are associated with values of $Q/Q_0 > 0.15$, thus with the presence of the most energetic structures. In the early acceleration very few u''–w'' events are observable, in conjunction with the absence of energetic vortex structures. At 30° the streamwise fluctuations dominate over the vertical ones associated with the presence of the quasi-streamwise structures of figure 17 at the same phase. From 45° to 135°, when turbulence is fully developed, most of the near-wall events lie within the II and IV quadrants related with the presence of the elongated and upward inclined structures visualized in figure 18. From about 135° the large-scale inclined structures tend to decay and consequently figure 19 shows the progressive reduction of the II–IV quadrant events up to their complete disappearance at 180°.

The above analysis has shown that from the late phases of the deceleration part of the half-cycle up to the early phases of the acceleration, turbulence appears to be less energetic and the shape of the coherent structures to be different from those developing over the remaining half-cycle. This can be attributed to the rise of the near-wall new laminar boundary layer in the reverse direction with respect to the previous half-cycle.

One question of interest is to understand whether the shape of turbulence (i.e. the shape of the energetic structures that are prevalent in the flow field) changes over the half-cycle. An effective tool for understanding such a feature is Lumley's map

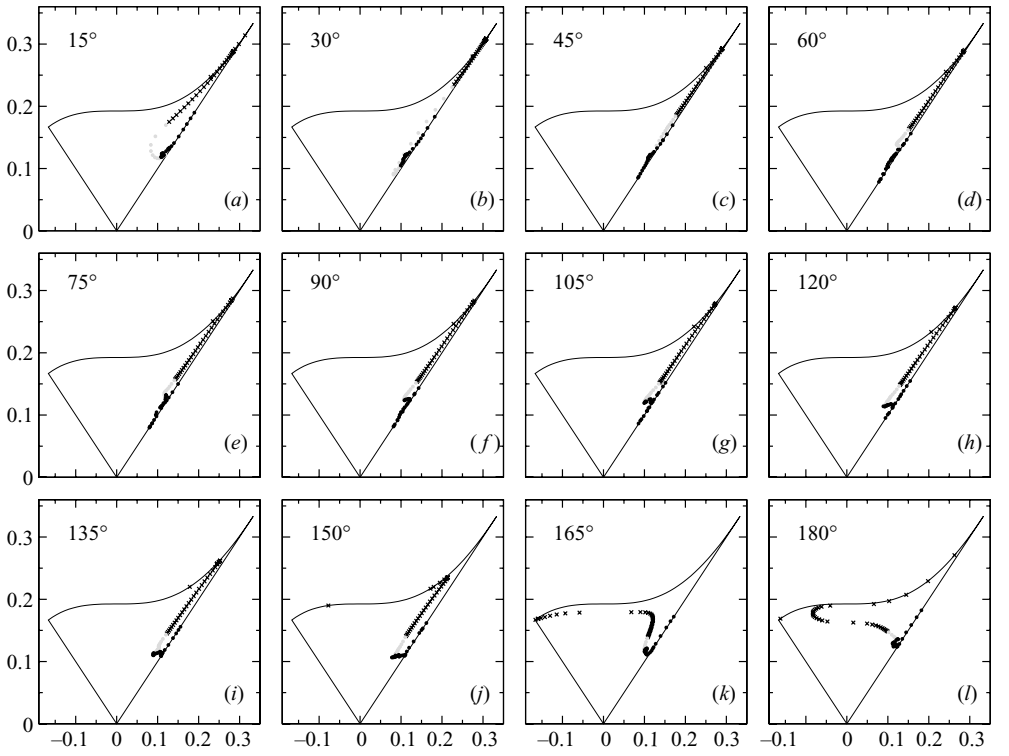

FIGURE 20. Anisotropy of the Reynolds stresses along a half-cycle shown using the Lumley invariant map: $0 < z_d/\delta_S < 1$ (crosses); $1 < z_d/\delta_S < 5$ (grey dots); $5 < z_d/\delta_S < 25$ (black dots). The horizontal axis is $III_b^{1/3}$, the vertical axis is $II_b^{1/2}$. Data from simulation C4.

(Lumley 1978) of the invariants of the anisotropy tensor:

$$b_{ij} = \frac{\langle u_i' u_j' \rangle}{2K} - \frac{1}{3}\delta_{ij}$$

with δ_{ij} the Kronecker symbol and K the turbulent kinetic energy. The square root of the second invariant ($II_b = -\frac{1}{2}\, b_{ij}b_{ji}$) quantifies the amount of anisotropy in the flow field, while the third root of the third invariant ($III_b = \frac{1}{3}\, b_{ij}b_{jk}b_{ki}$) gives the shape of the anisotropy. Lumley (1978) demonstrated that no turbulent state can lie outside the triangle of figure 20. The point (0, 0) represents isotropic turbulence. The lines originating from (0, 0) represent axis-symmetric turbulence: cigar-like on the right, meaning that one component prevails over the others; pancake-like on the left, meaning that two components have the same order of magnitude and prevail over the third one; the top line of the triangle represents two-component turbulence, where one of the three components is absent.

Figure 20 shows the vertical distribution of the turbulent states over half-cycle. As previously discussed, at the early stage of acceleration the near-wall region is characterized by the developing new laminar boundary layer, and the flow field characterized by the presence of weak large-scale slowly-decaying turbulent structures remaining from the previous half-cycle. This behaviour gives a near-wall region characterized by two-component turbulence (figure 20*a*) that gradually evolves toward a shape characterized by one component (streamwise) being larger than the other two, still

far from the canonical boundary layer shape (for comparison see figure 11.1 of Pope 2000). This corresponds to the fact that at these phases the vertical velocity fluctuations are much weaker than the horizontal ones (compare figure 13*a* with figures 11*a* and 12*a*) in the near-wall region. On the other hand, with increased distance from the wall, turbulence moves along the right-hand line toward the upper-right vertex of the triangle, namely along the cigar-like behaviour in the direction of one-dimensionality; this is due to the fact that toward the outer region, the cross-stream velocity fluctuations tend to decay much faster than the streamwise ones (compare the vertical distribution of u_{rms} in figure 6 with that of w_{rms} and v_{rms} in figures 7 and 8). At 30° (figure 20*b*) the presence of very long quasi-streamwise streaks (see figure 17) enhances the level of turbulent fluctuations in the three directions and the near-wall turbulence moves towards the canonical, cigar-like shape; the outer region behaves similarly to that at 15°. This different behaviour is due to the fact that turbulent motion is first originated in the near-wall region and progressively propagates upwards over the cycle (see also Hino *et al.* 1983). Specifically, at 30° the outer region is still characterized by the history effect already discussed, whereas the near-wall region is moving toward the sharp transition to turbulence. From 45° to 135° (figure 20*d–i*) the distribution of points resembles that of a boundary layer and the points representative of the log-layer (just below the knee) are clearly visible in the plots. In these cases we also observe that in the far field, similarly to the canonical wall turbulence, there is a trend toward isotropization, that is the points move along the right-hand line toward the origin of the axes. This behaviour is associated with the fact that the Reynolds shear stress as well as the differences among the three turbulent intensities tends to be smaller and smaller on going toward the outer region (see figures 5–8). At 150°–180° (figure 20*j–l*) the near-wall velocity reverses and a new thin boundary layer is growing in the reverse direction. Turbulence is present in the flow field due to the history effect already discussed. In this case the near-wall turbulence appears to have a clear two-component/pancake-like shape, whereas the far-field turbulence tends to decay more rapidly in the cross-stream direction than in the streamwise, and a trend toward the one-component state is detected (see figures. 11*d*, 12*d*, 13*d*). This behaviour can be associated with the decay of the vortical structures of figure 18.

To sum up, the analysis of the invariant map together with the spectra at $z_d = \delta_S$ and the phase distribution of the Reynolds stresses give the following scenario: in the central parts of the cycle where a fully developed turbulent regime is detected, the shape of turbulence is that of a canonical boundary layer; in the remainder of the cycle the near-wall turbulence has two-component/pancake-like characteristics, whereas the outer region tends toward one-dimensionality.

4. Performance of the SGS model

As previously stated in § 2 the subgrid-scale (SGS) stresses are modelled by means of a dynamic mixed model composed of an anisotropic scale-similar (*ss*) part and an eddy viscosity (*ev*) part. Such a model has been proved by many authors to be able to correctly simulate equilibrium as well as non-equilibrium flows. Among them, Shao, Sarkar & Pantano (1999) showed that the presence of a scale-similarity part properly takes into account the rapid-variable component of turbulence that depends explicitly on the mean shear, whereas the eddy-viscosity part reproduces the slow-variation component of turbulence not dependent on the mean velocity gradient. A dynamic eddy-viscosity model, with the constant averaged over the planes of homogeneity, was employed by Scotti & Piomelli (2001) to investigate pulsating

	$L_x/\delta_S, L_y/\delta_S, L_z/\delta_S$	$n_x \times n_y \times n_z$	$\Delta x^+, \Delta y^+, \Delta z^+_{min}, \Delta z^+_{max}$
DNS	$16\pi, 8\pi, 8\pi$	$128 \times 128 \times 96$	13, 6, 2, 27
LES	$16\pi, 8\pi, 8\pi$	$64 \times 64 \times 96$	26, 13, 2, 27
CDNS	$16\pi, 8\pi, 8\pi$	$64 \times 64 \times 96$	26, 13, 2, 27

TABLE 2. Computational parameters of the simulations at $Re_\delta = 990$. CDNS indicates the DNS simulation performed over the coarse grid.

channel flow in different flow regimes. When employed with a fine grid ($\Delta x^+ \sim 30$, $\Delta y^+ \sim 17$ based on the friction velocity of the steady component of the flow) the model gave results in good agreement with DNS data. This study has clearly shown the ability of the dynamic model to simulate flow fields characterized by a periodic sharp transition to turbulence and successive relaminarization. The scope of the present section is twofold: (i) to show the performance of the dynamic mixed model with the constant averaged over the planes of homogeneity (PADMM) in the case of a purely oscillating flow and considering two different flow regimes: the IT regime ($Re_\delta = 990$), where strongly non-equilibrium turbulence occurs over few phases in the cycle, and the turbulent regime already discussed ($Re_\delta = 1790$); (ii) to show that the SGS model affects the turbulent statistics only in the phases of the cycle where noticeable turbulent activity is detected.

4.1. $Re_\delta = 990$

This case was investigated experimentally by JSF89 (Test 6) and turbulent statistics are available for comparison with numerical data. We carried out three simulations, respectively a DNS, an LES and a coarse DNS (performed over the LES grid without the use of the SGS model). The DNS was carried out using $128 \times 128 \times 96$ grid cells respectively in the streamwise, spanwise and wall-normal directions. The LES and the coarse DNS were performed over $64 \times 64 \times 96$ grid points, with the same cell distribution in the wall normal direction as the DNS case and half the number of cells in the horizontal directions. The parameters of the simulations are in table 2. The results of the numerical simulations are compared with the available experimental data. The grid resolution herein employed for the DNS is the same as that of Vittori & Verzicco (1998), although the domain size in the horizontal directions is as large as twice as that of the simulations of Vittori & Verzicco (1998) and Costamagna *et al.* (2003).

The predicted ensemble-averaged wall shear stress is reported in figure 21 (experimental data are not available for this quantity). The late-deceleration to early-acceleration phases are predicted well by both the LES and the CDNS. These phases are characterized by the fact that a near-wall laminar boundary layer is developing and that the flow field is populated by large-scale structures remaining from the previous deceleration phases. The collapse of the numerical results indicates that: (i) the resolution of the coarse grid is sufficient to reproduce the flow field in these phases, characterized by the presence of few small scales (see Hino *et al.* 1983); (ii) in these phases the SGS stresses (not reported) are vanishingly small and the LES is equivalent to a DNS carried out over a coarser grid.

On the other hand, the PADMM fails to reproduce the sharp transition to turbulence and the associated rapid increase of the wall stress, occurring in the IT regime. The DNS gives a triangular-shaped behaviour of the wall shear stress in the phases where non-equilibrium turbulence occurs. This behaviour is typical of the

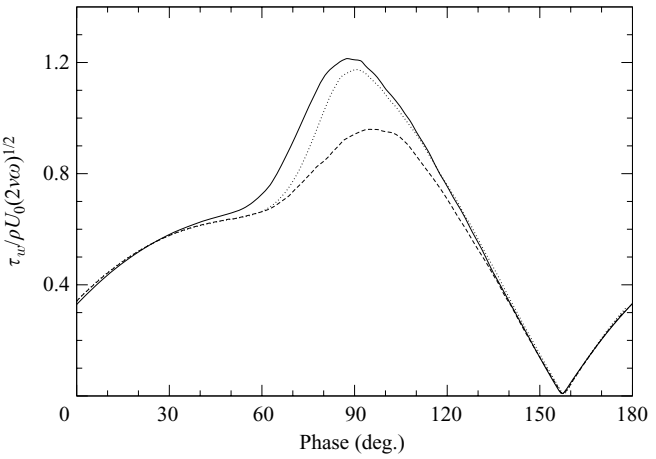

FIGURE 21. Ensemble-averaged wall shear stress along half-cycle in the IT regime ($Re_\delta = 990$): DNS (solid line), LES (dashed line), CDNS (dotted line).

IT regime (see for example figure 5*b* of Costamagna *et al.* (2003) which reports the experimental data of JSF89 at $Re_\delta = 1120$). The coarse DNS simulation is able to reasonably reproduce the sharp transition, thus proving that the grid resolution of the LES grid is fine enough; noticeable differences are obtained using the LES, which strongly delays transition and appreciably underpredicts the maximum value of the wall shear stress. The underprediction of the wall stress obtained with the LES can be attributed to the fact that in the IT regime the turbulent phases of the cycle are in strongly non-equilibrium conditions, and the underlying hypothesis of the standard DMM, namely the scale invariance, may be not suited for reproducing this kind of flow field. Another possible source of error may be the fact that in the IT regime turbulence appears strongly intermittent and in spots. For this reason plane averaging of the constant may not be suitable for reproducing such physics. A localized model, such as for example the Lagrangian one of Meneveau *et al.* (1996) may be better suited to reproduce the IT regime.

During the mid-deceleration phase, turbulence is decaying and the differences among the wall shear stress obtained in the three different simulations progressively decrease; finally the wall shear stresses of the three simulations collapse onto each other in the late deceleration phase, where the near-wall velocity has inverted sign and a new laminar boundary layer is forming in the reverse direction. At these phases, turbulent production is almost absent and, due to a memory effect, sparse large-scale structures remaining from the previous phases are present in the flow field (see Hino *et al.* 1983).

The analysis of the spectrum of the vertical fluctuation (figure 22) shows that at $Re_\delta = 990$ there are no phases where the universal Kolmogorov spectrum for E_{33} (see § 3) holds, thus clearly indicating the absence of equilibrium conditions and of an inertial subrange.

Figure 23 shows the DNS and LES mean velocity profiles (made non-dimensional with U_0) at four significant phases. Noticeable differences are evident in the near-wall region only, over the central phases of the cycle, where non-equilibrium turbulence is detected. The mean velocity profiles are affected by SGS modelling errors in the phases where turbulence activity is observed (between 70° and 135°), whereas the LES velocity profiles collapse onto the DNS ones in the remainder, where the contribution

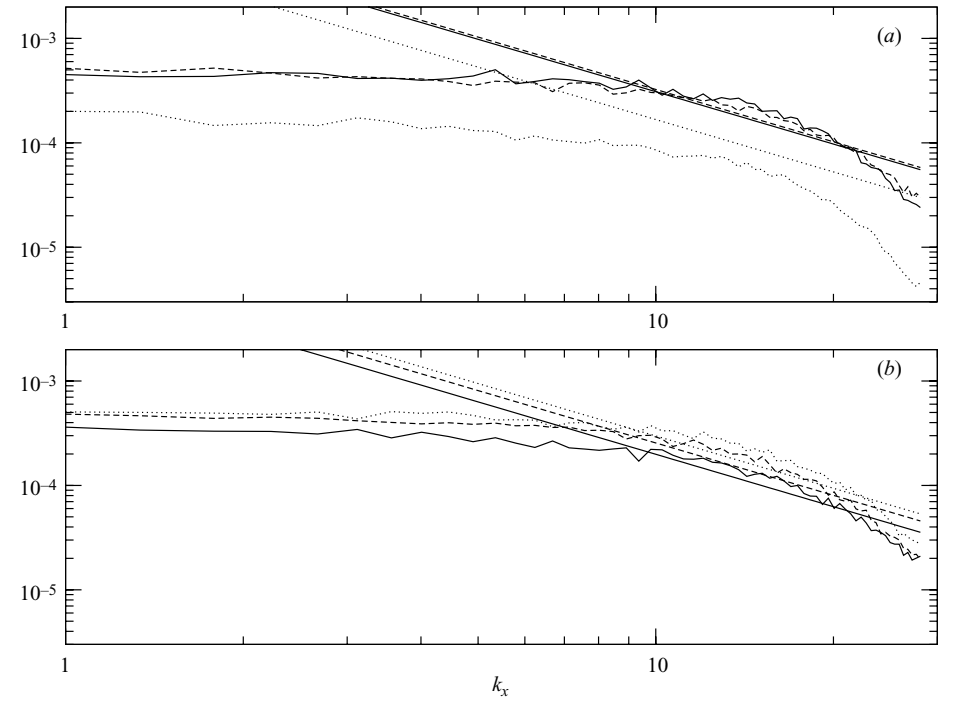

FIGURE 22. Spectra of dimensional resolved vertical fluctuation E_{33}/U_0^2 along the streamwise direction, at $z^+ = 80$: (*a*) 60^o (dotted line), 75^o (dashed line), 90^o (solid line); (*b*) 105^o (dotted line), 120^o (dashed line), 135^o (solid line). The straight lines are the isotropic Kolmogorov spectra $(24/55)C_s\epsilon^{2/3}k^{-5/3}$, with the dissipation rate ϵ calculated at the actual phases. $C_s = 1.5$ is the universal Kolmogorov constant (Sreenivasan 1995). Data from the DNS.

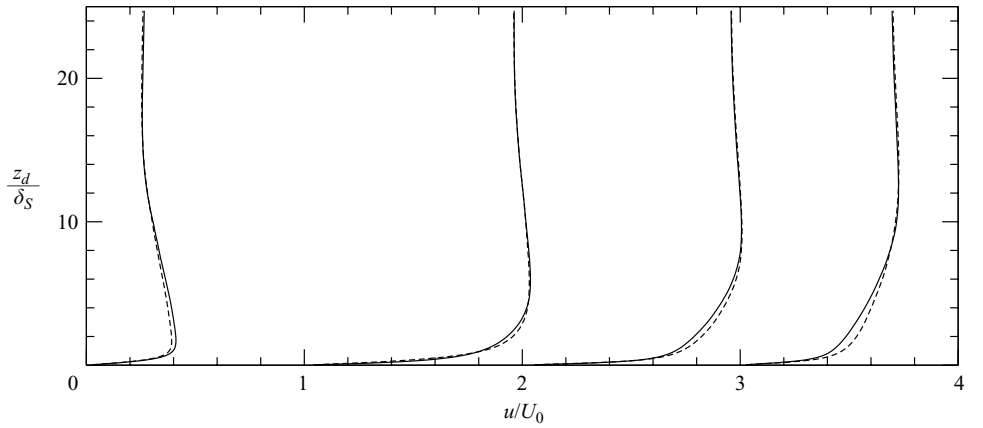

FIGURE 23. Ensemble-averaged profiles of the streamwise velocity at $Re_\delta = 990$: the quantities are made non-dimensional with outer variables. DNS, solid line; LES, dashed line. The profiles are plotted at 15°, 75°, 105° and 135°. For clarity the profiles are offset by 1 unit.

of the SGS stresses is very small. If the velocity profiles are scaled with inner variables (not shown here) the logarithmic velocity profile, previously observed in the T regime, is absent. This can be attributed to the non-equilibrium character of the highly intermittent and spotty turbulent phases of the IT regime.

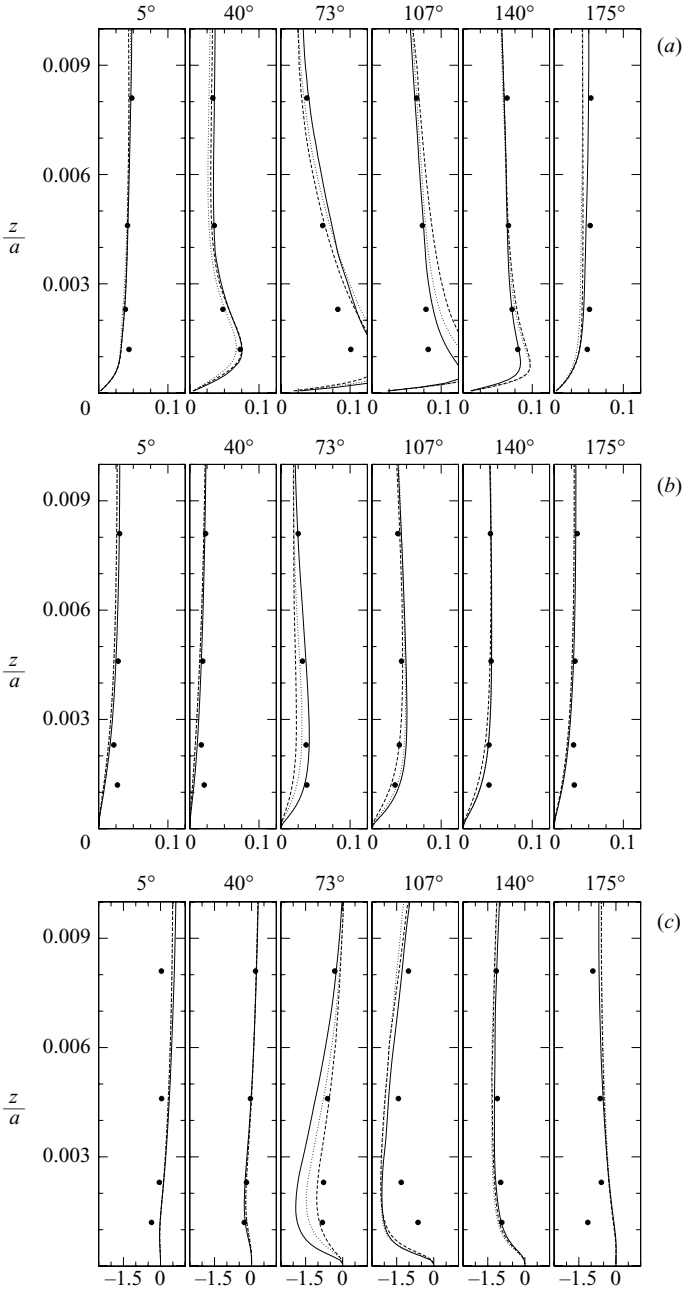

FIGURE 24. Second-order statistics over a half-cycle in the IT regime ($Re_\delta = 990$): (*a*) streamwise turbulent intensity; (*b*) wall-normal turbulent intensity; (*c*) Reynolds shear stress (DNS, solid line; LES, dashed line; CDNS, dotted line; experimental data by JSF89, dots).

The second-order statistics are shown in figure 24. As a general rule, the LES data collapse onto the DNS ones in all phases of the cycle other than the central ones. Differences between DNS and LES data are observable in the phases between 73° and 103° where the flow is in a non-equilibrium turbulent state. The strong discrepancy

between DNS and LES at 73° is consistent with the differences between wall shear stress predicted by the two simulations in the central phases (figure 21). As pointed out, this can be attributed to the fact that the PADMM is not designed for such non-equilibrium flow conditions, where turbulence appears in spots in the flow field.

A comparison between numerical (DNS) and experimental data shows disagreements in the wall-normal distribution of the Reynolds stresses. Note that the results of the present simulation are not affected by problems of domain size. Our domain size in the horizontal directions is twice that used in the DNS of Costamagna *et al.* (2003), and allows the two-point correlation functions to decay in less than half a domain length. For the streamwise intensity, large differences are detected in the turbulent phases of the half-cycle, whereas noticeable differences for the wall-normal turbulent intensity are evident in the near-wall region, especially in the range of phases between 140° and 40°. Finally, differences between DNS and experimental Reynolds shear stresses can be detected in the near-wall region, over the half-cycle. As already pointed out these differences may also be related to a high drop-out rate in the laser measurements (see JSF89). Based on the above discussion it can be argued that the disagreement in the Reynolds shear stress when comparing numerical data with experimental ones cannot be simply attributed to SGS modelling errors. As already discussed, more research is needed to detect the source of such disagreements.

4.2. $Re_\delta = 1790$

The increase of the Reynolds number reduces the characteristic time scale of turbulence compared to that of the oscillatory motion, thus allowing turbulence to adjust to a series of equilibrium states during the oscillation. As a consequence, as extensively shown throughout the paper, the PADMM is able to simulate correctly the Stokes boundary layer in the turbulent regime (see § 3). As widely shown and discussed in literature (for an exhaustive discussion see for example Piomelli 2004), when using a dynamic model, an increase of grid resolution reduces the contribution given by the SGS model to the turbulent quantities and makes the results closer to those of a DNS. Further, as we will clearly show in this section, in the phases of the cycle where the level of turbulent fluctuations is around its minimum, the contribution coming from the SGS model is almost absent.

In figure 25 vertical profiles of the Reynolds shear stress, the dissipation rate and eddy viscosity at 90° (when turbulence is at its maximum) are shown. As expected, the *ss* part, that takes into account for the unresolved, more energetic scales of turbulence, contributes much more to the composition of the Reynolds shear stress than the *ev* part (figure 25*a*). In particular, $\tau_{13,ss}$ contributes about the 18 % to the composition of the total shear stress $\langle u'w' \rangle$. A similar behaviour is observable for the dissipation rate (figure 25*b*). Specifically, most of the SGS dissipation rate of turbulent kinetic energy comes from the *ss* part of the model, consistently with the results obtained in steady wall-bounded turbulence by Armenio & Piomelli (2000). Since the *ss* part of the SGS Reynolds shear stress is much larger than the *ev* part, the SGS eddy viscosity associated with the *ss* part of the model is about one order of magnitude larger than that associated with the *ev* part of the model (figure 25*c*). The sum of the two SGS contributions is about one order of magnitude smaller than the resolved one, thus showing that, as usual in resolved LES, most of the turbulence scales are solved directly.

The distributions of the main SGS quantities along the vertical direction in the phases at which turbulence is fully developed are similar to those obtained in steady wall-bounded turbulence (see for instance Armenio & Piomelli 2000), thus

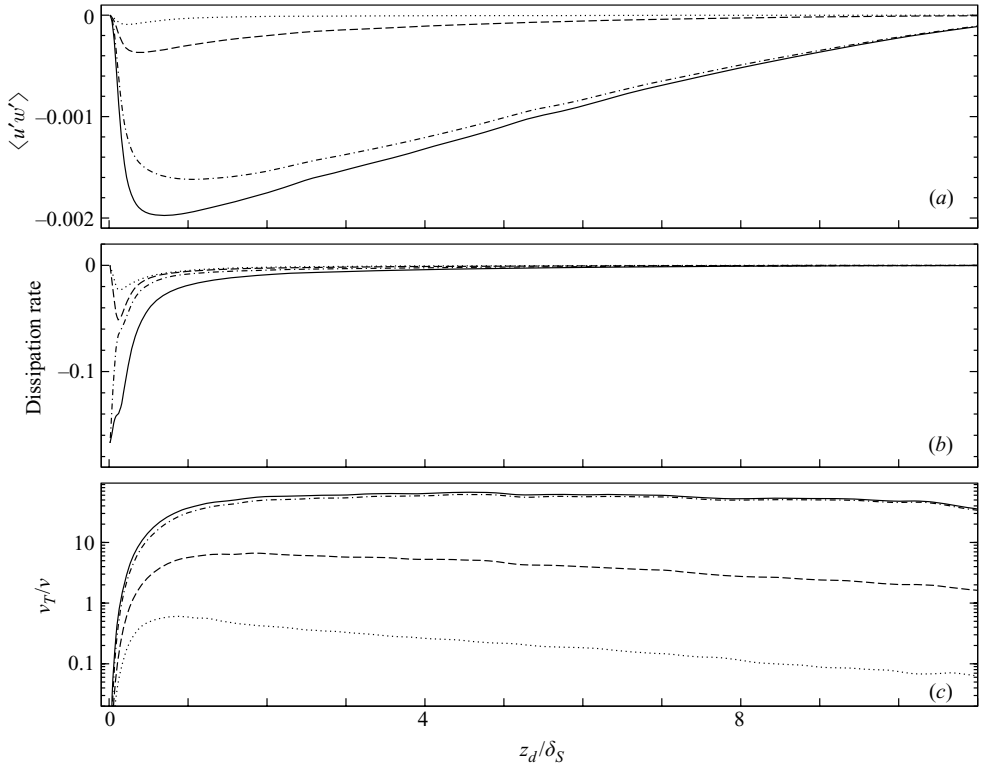

FIGURE 25. Vertical profiles at 90° of: (*a*) Reynolds shear stress: total ($\langle u'w' \rangle$, solid line); resolved ($\langle u''w'' \rangle$, dashed-dotted line); scale-similar part ($\tau_{13,ss}$, dashed line); eddy viscosity part ($\tau_{13,ev}$, dotted line). (*b*) Dissipation rate of resolved kinetic energy made non-dimensional with u_τ^4/ν: total (solid line); resolved (dash-dotted line); *ss* component (dashed line); *ev* component (dotted line). (*c*) Eddy viscosity to molecular viscosity ratio: total (solid line); resolved (dash-dotted line); *ss* component (dashed line), *ev* component (dotted line). Data from simulation C4.

showing that the dynamic mixed SGS model works properly in the simulation of unsteady oscillating flows when turbulence is fully developed, without requiring *ad hoc* modifications.

A more stringent test of the model is checking its ability to adapt to the local level of turbulence in those phases of the cycle where the inertial subrange is not observable and the level of turbulent fluctuations is around its minimum. In order to check these characteristics we analyse the evolution of the quantities discussed above over the cycle at a significant distance from the wall. Figure 26 shows that the dynamic model contributes to the composition of the Reynolds shear stress, the dissipation rate and the eddy viscosity consistently over the cycle. During the final phases of the deceleration part and the initial phases of the acceleration, consistently with the fact that turbulence activity is very small, and the small scales are almost absent (see Hino *et al.* 1983), the SGS Reynolds shear stress and the dissipation rate are vanishingly small. We also note that the SGS contributions to the eddy viscosity (figure 26*c*) decay much faster than the resolved one in the late deceleration phases (from 150°). This can be attributed to the physical characteristics of the flow field which in these phases exhibits few small scales, together with the presence of residual large-scale structures from the previous phases of the cycle. In the mid-acceleration phase, as turbulence

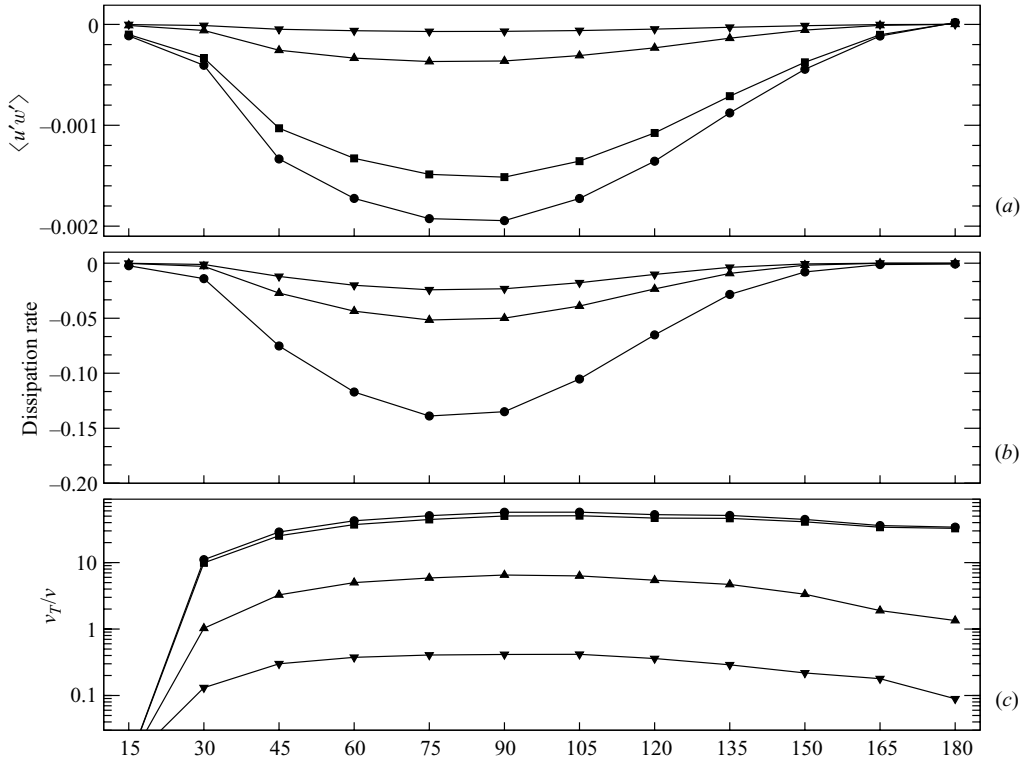

FIGURE 26. Mean values throughout the cycle: (*a*) Reynolds stress at $z_d \approx 0.5\delta_S$: total $\langle u'w' \rangle$ (●), $\langle u'w' \rangle - \langle u' \rangle \langle w' \rangle$ (■), $\langle u'w' \rangle_{ss}$ (▲), $\langle u'w' \rangle_{ev}$ (▼); (*b*) dimensionless dissipation at $z_d \approx 0.15\delta_S$: total (●), *ss* component (▲), *ev* component (▼); (*c*) normalized turbulent viscosity at $z_d \approx 2\delta_S$: total (●), *ss* component (▲), *ev* component (▼). Data from simulation C4.

activity increases, for example from 45°, the subgrid scales contribute proportionally to the development of the quantities discussed above, thus showing that the dynamic model adjusts properly to the actual level of turbulence and therefore supplies the contribution to turbulence from the small scales.

Finally we show in figure 27 the evolution over a half-cycle of the constant C of the model given in (2.5) at three significant distances from the bottom wall. The constant evolves throughout the half-cycle in agreement with the development of turbulent activity: very close to the wall it is practically zero in the late deceleration and early acceleration phases, according to the development of the near-wall laminar boundary layer. Small but non-zero values of C are observable from 170° to around 30° at $z^+ = 68$, due to the history effect previously discussed. Consistently with the sharp transition to turbulence and the associated generation of small scales, the constant C rapidly increases between 30° and 45° and then oscillates around a nearly constant value. Finally, C first drops to zero near the wall at 165°, where the inversion of the velocity profile occurs, whereas the decay is delayed in time as the distance from the wall increases, thus confirming that turbulence first decays near the wall and is still sustained in the outer region as a result of the presence of fully developed turbulence from the mid-deceleration phases.

4.3. *Discussion on the performance of the SGS model*

As a side result of the present research we have shown that the PADMM is able to simulate the Stokes boundary layer when quasi-equilibrium turbulence is present in

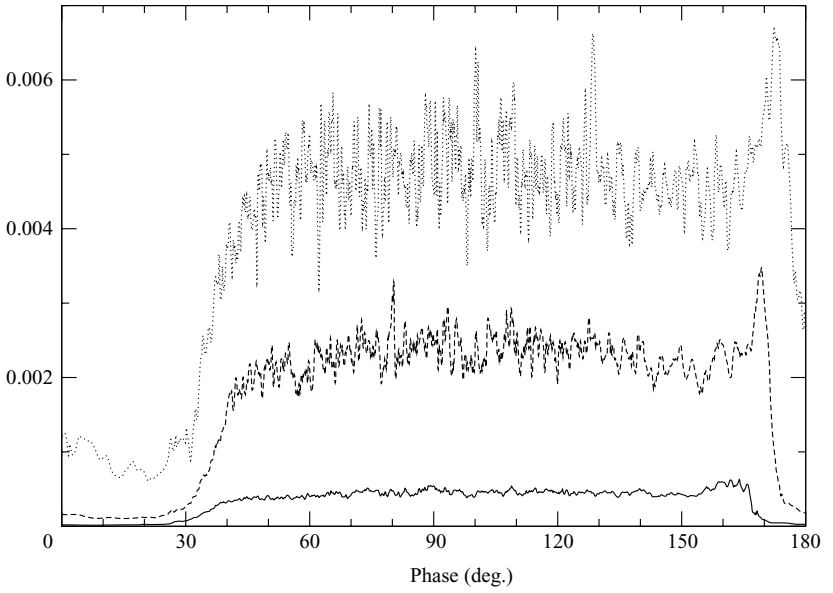

FIGURE 27. Evolution over a half-cycle of the constant C at $z^+ = 16$ (solid line), $z^+ = 33$ (dashed line) and $z^+ = 68$ (dotted line). Data from simulation C4.

the cycle of oscillation, whereas when strongly non-equilibrium turbulence appears over a few phases of the cycle, typical of the IT regime, the model is not able to reproduce correctly such phases. In order to understand better the range of application of the model in such a flow field, we analyse the results in the light of the relevant literature on the rapidly accelerated turbulent boundary layer. In particular, it has been established (see among others Greenblatt & Moss 2004 and Narasimha & Sreenivasan 1973) that depending on the size of the parameter

$$p^+ = -(\nu/\rho u_\tau^3)\frac{\mathrm{d}p}{\mathrm{d}x},$$

the flow can remain in local equilibrium, can lose equilibrium conditions and finally, can re-laminarize. The maximum pressure gradient can be calculated assuming that $\rho \mathrm{d}U/\mathrm{d}t = -\mathrm{d}p/\mathrm{d}x$ with U the time-evolving free-stream velocity. The parameter p^+ can be considered as the ratio between a turbulent inner-layer time scale ν/u_τ^2 and a free-stream time scale $[(1/u_\tau)\mathrm{d}U/\mathrm{d}t]^{-1}$. When p^+ is small the turbulent time scale is small and turbulence adjusts to local equilibrium conditions during the acceleration phase; for intermediate values the turbulent time scale increases and turbulence is characterized by strongly non-equilibrium conditions, and finally, a further increase of p^+ leads to relaminarization in the flow field. In Greenblatt & Moss (2004) three cases were studied in the three regimes discussed above, respectively characterized by $p^+ = 0.012, 0.019, 0.045$. Here we extend these findings to our case, which is characterized by the periodic variation of the forcing pressure gradient and thus by the fact that during the oscillation the parameter p^+ goes from ∞ (when $u_\tau = 0$) to 0, when the free-stream pressure gradient is zero (90°).

Figure 28 shows the parameter $|p^+|$ over a half-cycle for the simulation in the IT regime and in the T regime. In the T regime, we observe the presence of three distinct regions during the acceleration (from 0° to 90°). In the first part ($\infty > |p^+| > 0.02$) p^+ decreases along a curved line. This corresponds to the phases

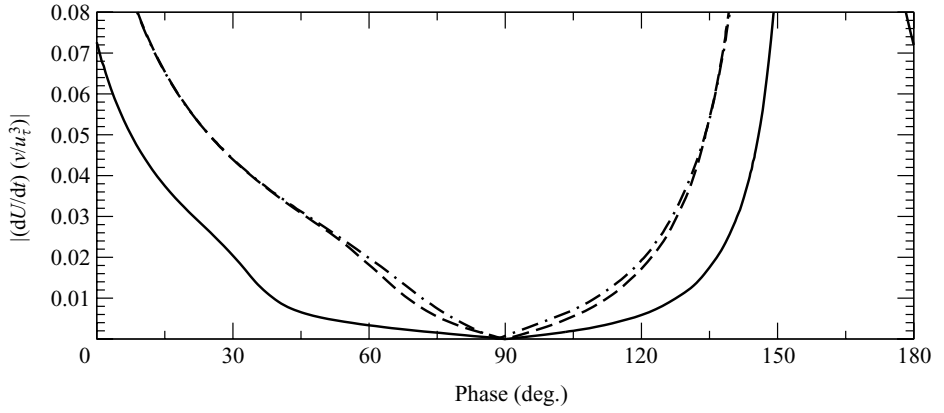

FIGURE 28. Mean evolution of the time scale ratio $|(dU/dt)(\nu/u_\tau^3)|$ for LES at $Re_\delta = 1790$ (solid line), DNS at $Re_\delta = 990$ (dashed line) and LES at $Re_\delta = 990$ (dashed-dotted line).

where a new boundary layer is just building up and, since the pressure gradient varies as $\cos t$ and $u_\tau \sim (\sin t)^{1/2}$, we have $p^+ \sim \mathrm{cotg}\, t/(\sin t)^{1/2}$. There is a second part where $0.02 > p^+ > 0.01$, characterized by having a constant large slope, where the flow is in the transitional phase, and a third phase, characterized by a gentle slope, $(0.01 > |p^+| > 0)$ where equilibrium conditions are reached. Note that the boundary between the regions roughly correspond to the values discussed by Greenblatt & Moss (2004).

In case of low Reynolds number (IT regime) the behaviour of $|p^+|$ is qualitatively different from that previously discussed. Specifically, the presence of the laminar region characterized by the curved line $(\infty > |p^+| > 0.02)$ is still detectable as well as the transitional region for $|p^+| < 0.02$. The main difference with the case $Re_\delta = 1790$ is the absence of a sharp change of slope at the value 0.01; rather we observe that $|p^+|$ goes from 0.02 to 0 along a curved line. This behaviour is associated with the presence of a range of phases characterized by non-equilibrium turbulence.

Based on these findings, the literature results on accelerated boundary layers can be reinterpreted and extended for the case of periodic forcing. In view of the fact that p^+ varies from ∞ to 0, irrespective of the value of Re_δ, *a priori* values defining the transition from one regime to another (for example from laminar to transitional phases) cannot be found. Rather we can distinguish one flow regime from another one based on the slope of $|p^+|(t)$. The laminar phases are characterized by a $\mathrm{cotg}\, t/(\sin\ t)^{1/2}$ behaviour. The transitional and the turbulent phases have different behaviour depending on the value of Re_δ. In the IT regime (low Re_δ value) the transitional phase starts at $p^+ \sim 0.02$ and it decreases to 0 at 90° along a curve. At large values of Re_δ (T regime) the transitional phase lies within $0.02 > |p^+| > 0.01$ and is characterized by a rapid decay of p^+, whereas the equilibrium turbulence phase $(0.01 > |p^+| > 0)$ goes along a line with gentle slope.

Now, we attempt to assess the performance and the range of application of the PADMM on the basis of the qualitative behaviour of $|p^+|$ over the acceleration phases:

(i) The PADMM is not suited to the simulation of the Stokes boundary layer in the IT regime, where equilibrium conditions are never reached during the half-cycle. This circumstance is demonstrated well by the fact that $|p^+|$ does not exhibit a sharp change of slope at 0.01.

(ii) The PADMM is able to simulate accurately the Stokes boundary layer in the T regime, where a large fraction of the oscillatory cycle is characterized by equilibrium turbulence and the transition to turbulence occurs very sharply. This behaviour is depicted by the sharp change of slope of $|p^+|$ at 0.01.

5. Concluding remarks

In the present work an LES study of the Stokes boundary layer in the turbulent regime at $Re_\delta = 1790$ was carried out. The subgrid-scale stresses were modelled through a plane-averaged dynamic mixed model. Owing to the burdensome computational efforts required for such a study, the code adopted was implemented in a parallel framework.

The statistics accumulated over 30 half-cycles of simulation were analysed and compared with the experimental data of test 8 of JSF89. Different computational grids and geometrical configurations were used. In the case of a perfectly flat wall, the fine-grid simulations C3–C5 supply a good estimation of the wall shear stress as well as of the turbulent intensities. The vertical profiles of the mean streamwise velocity and of the second-order statistics appear to be reproduced well during most of the phases of the half-cycle where equilibrium turbulence is present. Overall a very satisfactory agreement between numerical results and experimental data was obtained. Some disagreements between numerical and experimental vertical turbulent intensities appeared in the phases of the cycle between 160° and 30°, and for the r.m.s. of the wall shear stress in the central part of the half-cycle. Such disagreements were found not to be dependent either on the imposition of a shear-free surface at the top of the domain or on the presence of small-amplitude wall imperfections. On the other hand, an analysis of the literature suggests that disagreements between numerical (DNS) results and experimental data are observed when comparing second-order statistics in such kinds of flow. Additional simulations carried out in the IT regime at $Re_\delta = 990$ show that disagreements are also present when comparing DNS with experimental data. Since our LES with a dynamic model asymtotically converges toward DNS with increased grid resolution, one may argue that such disagreements are not simply due to SGS modelling. This issue deserves more research.

Our fine-grid computations correctly simulated the evolution of turbulence over the alternation of acceleration and deceleration phases in the cycle of oscillation. Specifically, a rapid increase of turbulent kinetic energy was observed between 30° and 45°, associated with the sudden increase of the production rate of K. Fully developed equilibrium turbulence appeared between 60° and 150°–160°. From 165° a new near-wall laminar boundary layer develops in the reverse direction, whereas due to a history effect few large-scale structures from the previous phases populate the fluid column. The new near-wall laminar boundary layer continues to develop through the early acceleration phase up to 30°–45°, when a new sharp transition to turbulence is observed. Our analysis is fully consistent with the findings of the experimental study of Hino *et al.* (1983) in the IT regime and with those of JSF89 in the IT–T regimes.

In the phase interval between 60° and 150° the following features were observed: the mean velocity profiles are characterized by the presence of a log-layer, similar to that of a canonical steady boundary layer; the one-dimensional energy spectra exhibit a very short, but still detectable, inertial range obeying the Kolmogorov universal law with constant $C_s = 1.5$. The maxima of the production and dissipation rates of the turbulent kinetic energy, scaled with inner variables, are very close to those of a

steady plane channel flow at $Re_\tau = 180$. These findings clearly indicate that once fully developed conditions are reached, the turbulent phases evolve over the cycle through a series of quasi-equilibrium states, resembling those of an equivalent steady boundary layer.

An analysis of the space–time distribution of the Reynolds stresses, of the energy spectra, of the instantaneous coherent structures, and of the map of anisotropy of the Reynolds stresses has shown the presence of two different regions in the flow field, namely a near-wall region ($z_d < 5\delta_S$) and an outer one ($z_d > 5\delta_S$).

In the near-wall region, elongated streaks nearly equi-spaced along the spanwise direction are generated around 15°, their mean spacing of 110 wall units being in agreement with the literature data; then they coalesce and successively break up into smaller structures. Such dynamics appears similar to that observed in the IT regime by other authors, apart from the fact that the phase at which the elongated streaks are formed and successively break up, appears shifted back to well before the beginning of the deceleration part. As also explained in JSF89, this can be attributed to a Reynolds number effect. The mechanism of streak formation, successive coalescence and eventual destruction appears similar to that observed by Scotti & Piomelli (2001) for a pulsating flow in the current-dominated and low-frequency regime, when the amplitude of the oscillation is large enough to give relaminarization and successive re-transition to turbulence in the flow field. As also argued by Scotti & Piomelli (2001), this appears to be a feature of an unsteady flow which undergoes periodic re-transition to turbulence, rather than an inherent characteristic of the Stokes boundary layer. Our results also give support to the intuition of Sarpkaya (1993), who asserted that there must be a value of the shear Reynolds number around 20–28 beyond which elongated and regular structures break up into a population of small ones giving rise to the production of smaller and smaller scales. Specifically we find that the criterion applied using the ensemble-averaged value of the wall shear stress gives the phase at which the breaking of the structures is expected in the cycle. From around 160° a new laminar boundary layer is estabilished in the reverse direction and it develops in a laminar state up to the early acceleration phases. At these phases large-scale residual turbulent structures, from the energetic phases of the cycle, are present in the fluid column. In the near-wall region the development of the laminar boundary layer tends to destroy vertical turbulent fluctuations at a larger rate than the horizontal ones, thus giving rise to two-component/pancake-like turbulence.

The outer region, from 45° to 135°, behaves similarly to that of a canonical boundary layer, since turbulence tends to move toward isotropy far from the wall. On the other hand, from 135° to 30° the opposite is true, in that two components of turbulence, namely the cross-stream ones, tend to decay faster than the streamwise one, thus giving rise to a shape that moves towards the one-component turbulence.

As already proved by Scotti & Piomelli (2001) the plane-averaged dynamic SGS model is able to simulate periodically driven turbulent flows even when part of the cycle of oscillation is in a laminar state. Our results show that the PADMM correctly reproduced the Stokes boundary layer in the T regime. As a side result of the present research, the performance of the SGS model was also evaluated in the IT regime, where the flow field is in a laminar state over most of the cycle, and non-equilibrium turbulence occurs over a few phases from late acceleration to mid deceleration. In this case the model was not able to simulate correctly the turbulent phases of the cycle. This may be attributed to two main reasons: (i) the underlying hypothesis of the DMM (namely scale invariance) does not hold in strongly non-equilibrium conditions; (ii) plane averaging of the constant is not suitable in the IT regime where

turbulence appears to be highly intermittent and spot-like in time and in space. The use of localized models may be beneficial at such a condition. The range of application of the PADMM was assessed based on the evolution along the phases of acceleration of the non-dimensional parameter p^+ that can be interpreted as the ratio between a turbulent time scale and an inertial time scale. The PADMM works successfully when a sharp change of the slope of the time evolution of p^+ occurs at 0.01. From a physical point of view this corresponds to the developing of equilibrium turbulence.

We wish to thank Professor M. Sumer for having kindly provided his experimental data. The present research has been financially supported by the Istituto di Oceanografia e di Geofisica Sperimentale – OGS. The numerical computations have been carried out on the IBM-SP4 facility of CINECA (Bologna, Italy).

REFERENCES

Akhavan, R., Kamm, R. D. & Shapiro, A. H. 1991*a*. An investigation of transition to turbulence in bounded oscillatory Stokes flows. Part 1. Experiments. *J. Fluid Mech.* **225**, 395.

Akhavan, R., Kamm, R. D. & Shapiro, A. H. 1991*b*. An investigation of transition to turbulence in bounded oscillatory Stokes flows. Part 2. Numerical simulations. *J. Fluid Mech.* **225**, 423.

Armenio, V. & Piomelli, U. 2000 A Lagrangian mixed subgrid-scale model in generalized coordinates. *Flow Turbulence Combust.* **65**, 51.

Armenio, V. & Sarkar, S. 2002 An investigation of stably-stratified turbulent channel flow using large eddy simulation. *J. Fluid Mech.* **459**, 1.

Armenio, V. & Sarkar, S. 2004 Mixing in a stably-stratified medium by horizontal shear near vertical walls. *Theor. Comp. Fluid Dyn.* **17** (5–6).

Bardina, J., Ferziger, J. H. & Reynolds, W. C. 1980 Improved subgrid scale models for large eddy simulation. *AIAA Paper* 80-1357.

Blondeaux, P. & Seminara, G. 1979 Transizione incipiente al fondo di un'onda di gravitá. *Rend. fisici Accad. Lincei*, serie 8, **LXVII**.

Calhoun, R. J. & Street, R. L. 2001 Turbulent flow over a wavy surface: Neutral case. *J. Geoph. Res.* **106** (C5), 9277.

Costamagna, P., Vittori, G. & Blondeaux, P. 2003 Coherent structures in oscillatory boundary layers. *J. Fluid Mech.* **474**, 1.

Cui, A. & Street, R. L. 2001 Large-eddy simulation of turbulent rotating convective flow development. *J. Fluid Mech.* **447**, 53.

Ding, L. & Street, R. L. 2003 Numerical study of the wake structure behind a three-dimensional hill. *J. Atmos. Sci.* **60**, 1678.

Dubief, Y. & Delcayre, F. 2000 On coherent-vortex identification in turbulence. *J. Turbulence* **3**, 008.

Falcomer, L. & Armenio, V. 2002 Large-eddy simulation of secondary flow over longitudinally-ridged walls. *J. Turbulence* **1**, 011.

Fredsøe, J., Sumer, B. M., Laursen, T. S. & Pedersen, C. 1993 Experimental investigation of wave boundary layers with a sudden change in roughness. *J. Fluid Mech.* **252**, 117.

Germano, M., Piomelli, U., Moin, P. & Cabot, W. H. 1991 A dynamic subgrid-scale eddy viscosity model. *Phys. Fluids* A **3**, 1760.

Greenblatt, D. & Moss, E. 2004 Rapid temporal acceleration of a turbulent pipe flow. *J. Fluid Mech.* **514**, 65.

Gullbrand, J. & Chow, F. K. 2003 The effect of numerical errors and turbulence models in large-eddy simulations of channel flow, with and without explicit filtering. *J. Fluid Mech.* **495**, 323.

Henn, D. S. & Sykes, R. I. 1999 Large eddy simulation of flow over wavy surfaces. *J. Fluid Mech.* **383**, 75.

Hino, M., Kashiwayanagi, M., Nakayama, A. & Hara, T. 1983 Experiments on the turbulence statistics and the structure of a reciprocating oscillatory flow. *J. Fluid Mech.* **131**, 363.

Hino, M., Sawamoto, M. & Takasu, S. 1976 Experiments on transition to turbulence in an oscillatory pipe flow. *J. Fluid Mech.* **75**, 193.

Hsu, C.-T., Lu, X. & Kwan, M.-K. 2000 LES and RANS studies of oscillating flows over flat plate. *Trans. ASCE: J. Engng Mech.* **126**, 186.

Hunt, J. C. R., Wray , A. A. & Moin, P. 1988 Eddies, streams and convergence zones in turbulent flows. *Center of Turbulence Research (Proc. Summer Program, 1988)*, p. 193.

Jensen, B. L., Sumer, B. M. & Fredsøe, J. 1989 Turbulent oscillatory boundary layers at high Reynolds numbers. *J. Fluid Mech.* **206**, 265.

Kamphuis, J. W. 1975 Friction factor under oscillatory waves. *J. Waterways, Port Coastal Engng Div. ASCE* **101** (WW2), 135.

Lam, K. & Banerjee, S. 1992 On the condition of streak formation in a bounded turbulent flow. *Phys. Fluids* A **4**, 306.

Lilly, D. K. 1992 A proposed modification of the Germano subgrid-scale closure method. *Phys. Fluids* A **4**, 633.

Lodahl, C. R., Sumer, B. M. & Fredsøe, J. 1998 Turbulent combined oscillatory flow and current in a pipe. *J. Fluid Mech.* **373**, 313.

Lohmann, I., Fredsøe, J., Sumer, B. M. & Christiensen, E. D. 2006 Large eddy simulation of the ventilated wave boundary layer. *J. Geophys. Res. – Oceans* **111**, CO6036, doi:10.1029/2005JC002946.

Lumley, J. L. 1978 Computational modelling of turbulent flows. *Adv. Appl. Mech.* **18**, 123.

Lund, T. S. 1997 On the use of discrete filters for large eddy simulations. *Annual Research Briefs 1997*, p. 83. Center for Turbulence Research, NASA Ames-Stanford University.

Lund, T. S. & Kaltenbach, H.-J. 1995 Experiments with explicit filtering for LES using a finite-difference method. *Annual Research Briefs 1995*, p. 91. Center for Turbulence Research, NASA Ames-Stanford University.

Mansour, N. N., Kim, J. & Moin, P. 1988 Reynolds-stresses and dissipation-rate budgets in a turbulent channel flow. *J. Fluid Mech.* **194**, 15.

Meneveau, C., Lund, T. S. & Cabot, W. H. 1996 A Lagrangian dynamic subgrid-scale model of turbulence. *J. Fluid Mech.* **319**, 353.

Moin, P. & Mahesh, K. 1998 Direct numerical simulation: a tool in turbulence research. *Annu. Rev. Fluid Mech.* **30**, 539.

Narasimha, R. & Sreenivasan, K. R. 1973 Relaminarization in higly accelerated turbulent boundary layers. *J. Fluid Mech.* **61**, 417.

Piomelli, U. 2004 Large eddy and direct simulation of turbulent flows. In *Introduction to Turbulent Modeling V*, VKI Lecture Series 2004–06

Piomelli, U. & Balaras, E. 2002 Wall-layer models for large-eddy simulations. *Annu. Rev. Fluid Mech.* **34**, 349.

Pope, S. B. 2000 *Turbulent Flows*. Cambridge University Press.

Robinson, S. K. 1991 Coherent motions on the turbulent boundary layer. *Annu. Rev. Fluid Mech.* **23**, 601.

Sarghini, F., Piomelli, U. & Balaras, E. 1999 Scale similar models for large-eddy simulations. *Phys. Fluids* **11**, 1596.

Sarpkaya, T. 1993 Coherent structures in oscillatory boundary layers. *J. Fluid Mech.* **253**, 105.

Scotti, A. & Piomelli, U. 2001 Numerical simulation of pulsating turbulent channel flow. *Phys. Fluids* **13**, 1367.

Shao, L., Sarkar, S., Pantano, C. 1999 On the relationship between the mean flow and subgrid stresses in large eddy simulation of turbulent shear flows. *Phys. Fluids* **11**, 1229.

Smagorinsky, J. 1963 General circulation experiments with the primitive equations. I. The basic experiment. *Mon. Weath. Rev.* **91**, 99.

Spalart, P. R. & Baldwin, B. S. 1987 Direct simulation of a turbulent oscillating boundary layer. *Turbulent Shear Flows 6* Springer.

Spalart, P. R., Jou, W.-H., Strelets, M. & Allmaras, S. R. 1997 Comments on the feasibility of LES for wings, and on a hybrid RANS/LES approach. *First AFOSR Int. Conference on DNS/LES, Ruston, LA, 4–8, August 1997*, In *Advanced in DNS/LES* (ed. C. Liu & Z. Liu) Greyden, Columbus, OH.

Sreenivasan, K. R. 1995 On the universality of the Kolmogorov constant. *Phys. Fluids* **7**, 2778.

Sumer, B. M., Laursen, T. S. & Fredsøe, J. 1993 Wave boundary layers in a convergent tunnel. *Coastal Engng.* **20**, 317.

Vittori, G. & Verzicco, R. 1998 Direct simulation of transition in an oscillatory boundary layer. *J. Fluid Mech.* **371**, 207.

Vreman, B., Guerts, B. & Kuerten, H. 1994 On the formulation of the dynamic mixed subgrid-scale model. *Phys. Fluids* **6**, 4057.

Wallace, J. M., Eckelmann, H. & Brodkey, R. S. 1972 The wall region in turbulent shear flow. *J. Fluid Mech.* **54**, 39.

Wu, X. & Squires, K. D. 1998 Numerical investigation of the turbulent boundary layer over a bump. *J. Fluid Mech.* **362**, 229.

Zang, Y., Street, R. L. & Koseff, J. R. 1994 A non-staggered grid, fractional step method for time-dependent incompressible Navier-Stokes equations in curvilinear co-ordinates. *J. Comput. Phys.* **114**, 18.